1 Solar radiative transfer and global climate modelling

H. W. Barker

1.1 Introduction

Over a period of time, Earth's outer shell (atmosphere, hydrosphere, cryosphere, biosphere) winds along a unique trajectory toward an ever-changing, and hence elusive, radiative equilibrium. It is elusive partly because Earth's overwhelming external boundary condition, solar irradiance, is never constant thanks to continuous variations in both orbit about the Sun and solar output. As such, the best Earth, and any other planet, can do is achieve a sequence of states that are in quasi- (radiative) equilibrium over a period of time that spans at least several annual cycles. Even if boundary conditions were static, it is now recognized that Earth's climate would not settle down to a single state or even a fixed cycle. Instead, it would execute a non-repeating sequence of, potentially very diverse, states that approximate radiative equilibrium. This chaotic character is supported by the inexorable intertwining of internal processes that operate at radically different time-scales. Indeed, the life giving/supporting character of Earth's climate system, that begins with absorption of solar radiation and ends with infrared emission to space, owes much of its richness, and worthiness of study, to the four-dimensional interaction between radiation and the three phases of water.

Given the fundamental role of large-scale radiation budgets in setting the character of climate and climatic change, and the fact that large-scale budgets are governed by conditions at smaller scales, it is essential that radiation–water interactions be accounted for as accurately as possible in numerical global climate models (GCMs). In GCMs, however, physical processes that occur at scales less than several hundred kilometres are often unresolved and so must be parametrized in terms of resolved conditions and assumptions about the state of unresolved conditions. This includes radiative transfer and many atmospheric fluctuations as their characteristic scales are typically less than a few kilometres.

While radiative fluxes at specific wavelengths are important for certain processes, such as photosynthesis, the primary role played by radiation within the climate system is heating and cooling. Hence, for the most part, modelling the flow of radiation in a dynamical model of Earth involves integrations of fluxes over fairly broadbands. Broadband irradiances, or fluxes, are generally defined for incoming solar radiation and terrestrial radiation emitted by the Earth–atmosphere system. While these sources overlap, they are generally considered to be exclusive and to span wavelengths between $[0.2, 5]$ μm for solar and $[5, 50]$ μm for terrestrial. Like their counterparts in the spatial domain, atmospheric spectral properties have to be defined at fairly course resolutions for radiation calculations in GCMs.

Given that the central topic of this volume is scattering of light, and the fact that solar radiation is scattered in the Earth–atmosphere system to a much greater extent than terrestrial radiation[1], this chapter focuses overwhelmingly on the treatment of solar radiative transfer within GCMs. Hence, the purpose of this chapter is to briefly review methods for computing solar radiative transfer in GCMs and to speculate on both deficiencies in these methods and how far we should be going to address these deficiencies.

The second section of this chapter gives a brief overview of how radiation figures into the climate system and the important role that radiation plays in diagnosing both real and modelled climates. The third section presents the basic method of representing solar radiative transfer in GCMs; two-stream approximations. It also discusses methods that have been proposed to extend two-streams in order that they capture the essence of solar transfer through unresolved inhomogeneous cloudy atmospheres. In the fourth section, 1D (i.e., two-stream-based) solar transfer is contrasted with 3D transfer and it is asked whether global modellers should be concerned about systematic differences. The fifth section highlights some recent work with remote sensing of cloudy atmospheres. Concluding remarks are made in the final section.

1.2 Earth's radiation budget and feedbacks

This section provides an overview of the central role played by radiation in global climatology. It discusses the impact of clouds on Earth's radiation budget and the prominent role of radiation in cloud–climate feedback processes.

1.2.1 Earth's radiation budget and climatic variables

The fundamental working hypothesis in analysis of global climate is that over a sufficiently long period of time T (> 1 year), the Earth–atmosphere system is in radiative equilibrium such that

$$\int_T \left\{ \frac{S_\odot(t)}{4} \left[1 - \alpha_p(t)\right] - \mathcal{I}(t) \right\} \mathrm{d}t = 0, \tag{1.1}$$

[1] Rayleigh scattering is effectively nil at terrestrial wavelengths and the imaginary part of the refractive index for water in the heart of the solar spectrum is several orders of magnitude smaller that it is in the atmospheric thermal window.

where $S_\odot$ is incoming normal solar irradiance (according to the SORCE radiometer, $S_\odot \approx 1361 \pm 0.5\,\mathrm{W\,m^{-2}}$ at 1 AU; see http://lasp.colorado.edu/sorce/tsi_data.html), the factor of 1/4 arises because Earth is spherical, α_p is top of atmosphere (TOA) albedo, and $\mathcal{I}$ is outgoing longwave radiation (OLR). All of the quantities in (1.1) are spectrally-integrated. Climatic variables are often grouped into two classes: *external* and *internal* variables. External variables are those that evolve independently of climate. That is, they affect an effect, but there are no return effects. The ultimate external variable is of course $S_\odot$. Through variations in Earth's orbit about the Sun and variations in solar output (both spectrally and integrated), $S_\odot$ varies constantly (see the SORCE page listed earlier). Volcanic activity is often cited as an external variable. On sub-geologic time-scales this is accurate as volcanic emissions can impact α_p significantly with no discernible reverse impact on volcanic activity. On much longer time-scales, however, volcanoes alter atmospheric composition and it has been speculated that this alters life, ocean sediments, the lithosphere, plate tectonics, and hence volcanic activity (Lovelock 1988).

If a fluctuating variable exhibits excessive intermittency it can fall into a grey zone between internal and external. For instance, desert dust storms, which can alter the vertical distribution of radiation significantly over large regions, are highly intermittent. One could argue that dust storms only impact weather and climate and that their rate and frequency of occurrence does not depend on themselves. But where does one draw the line and impose a threshold? Since the distribution of dust storms depends on local conditions that are naturally tied to large-scale conditions, then since dust storms influence weather, there must be a direct link back to their occurrence. While many factors conspire to bring about a certain distribution of dust storms, dust storms themselves must play a role and so dust storms are not external variables, despite the seeming gulf between their immediate impacts and their sources.

Another grey variable is human activity. On one hand, climate determines greatly the distribution of human settlement and activity. It has been known for many decades that human activity can directly impact climate, as exemplified in studies of desertification (Charney et al. 1977), deforestation (Snyder et al. 2004), and greenhouse gas emissions (Houghton et al. 2001). Desertification and deforestation result in direct alterations to surface albedo, surface roughness, and evapotranspiration. This has direct impacts on local partition of energy available for heat and water fluxes. These alter circulation and moisture patterns and hence local and global climate. Emissions of greenhouse gases alter atmospheric opacity and hence $\mathcal{I}$. The short to medium term impacts on global climate have been studied widely, and while the gross details are recognized generally, specifics (i.e., regional impacts) are still unclear. So, for example, if desertification and deforestation alter regional and global climate, and these alterations force changes in agricultural and silvicultural practices (i.e., human activity), human activity will then be undoubtedly an internal variable. Likewise, if the impacts of global warming via increased levels of greenhouse gases alter human activity, humans are again an internal variable. Indeed, it is difficult to imagine how life in general can be anything other than an internal variable.

An indisputable example of an internal climatic variable is cloud. Clouds are highly intermittent, like dust storms, exist over a wide range of spatial and temporal scales, and demonstrably influence, and get influenced by, their environment. While each cloud, and field that it is associated with, is an individual example, their properties are generally discussed in climatology in terms of spatial and temporal integrals and hence as members of a population. Clearly there is an overall population of clouds, but often clouds are categorized into subpopulations in terms of the meteorological conditions in which they live. As climate fluctuates, correlations of distributions of occurrence of cloud subpopulations can change and so too can the internal characteristics of subpopulations. In the former case, clouds are clouds and it is frequencies of occurrence of subpopulations that fluctuate in space and time. For example, a region subject to a changing climate might experience more cumuliform clouds and fewer stratiform clouds, yet the characteristics of each subpopulation might remain unchanged. In the latter, detailed properties of clouds might change presumably along with changes to frequency distributions of subpopulations. For example, a drier climate might have more wind-blown dust which might alter particle size, turbulent structure, and vertical extent of cumuliform clouds. Changes to subtle properties like these will impact local energy and moisture budgets, circulation, dust occurrence, subtle cloud properties, and ultimately frequencies of occurrence of cloud subpopulations. Either way, the role of clouds, as internal variable, in climate and climatic change is still very murky. Hence, uncertainty about representation of their structural and radiative properties in climate models diminishes confidence in climate model predictions (Houghton et al. 2001).

1.2.2 Radiation and climate feedbacks

Conventionally, climate sensitivity has been assessed by assuming that (1.1) holds and that perturbations to (1.1) by amounts ΔR, arising from changing either an internal or external variable, are sudden and followed by restoration of equilibrium so that (1.1) holds again. In actuality, ΔR are generally time-dependent (i.e., forcings are generally transient) thereby inexorably intertwining forcing(s), restoration of equilibrium, and internal chaotic behaviour.

Aires and Rossow (2003) developed a general multivariate expression for the time evolution of changes to TOA net flux F. For brevity and simplicity, discussion of their formulation picks up after several basic assumptions have been made that limit the nature, and make for more tractable analyses, of the climate system. Assume that a time-dependent external forcing ΔR is applied to the climate system and that it acts only on F. Thus, ΔR represents a radiative perturbation such as, for example, a change to the solar constant or a volcanic eruption. This results in changes to internal climatic variables x_i that interact with one another and thus alter F further. Aires and Rossow expressed the change in F as a function of time t as

$$\Delta F\left(t_0+2\Delta t\right) \approx \Delta R\left(t_0+2\Delta t\right)+\sum_i \frac{\partial F\left(t_0+2\Delta t\right)}{\partial x_i\left(t_0+\Delta t\right)}\Delta x_i\left(t_0+\Delta t\right) \quad (1.2)$$
$$+\sum_i\sum_j \frac{\partial F\left(t_0+2\Delta t\right)}{\partial x_i\left(t_0+\Delta t\right)}\frac{\partial x_i\left(t_0+\Delta t\right)}{\partial x_j\left(t_0\right)}\Delta x_j\left(t_0\right),$$

where Δt is timestep. A large step towards classical analysis of climate models is to assume that the external forcing ΔR on F directly impacts a single *diagnosed* variable, considered here (and most often) to be surface air temperature T_s, with negligible direct impact on other variables. This simplifies (1.2) to

$$\Delta F\left(t_0+2\Delta t\right) \approx \Delta R\left(t_0+2\Delta t\right)+\frac{\partial F\left(t_0+2\Delta t\right)}{\partial T_s\left(t_0+\Delta t\right)}\Delta T_s\left(t_0+\Delta t\right) \quad (1.3)$$
$$+\sum_i \underbrace{\underbrace{\frac{\partial F\left(t_0+2\Delta t\right)}{\partial x_i\left(t_0+\Delta t\right)}}_{\substack{\text{radiative}\\ \text{sensitivities}}}\underbrace{\frac{\partial x_i\left(t_0+\Delta t\right)}{\partial T_s\left(t_0\right)}}_{\substack{\text{state}\\ \text{relations}}}}_{\text{feedbacks}}\Delta T_s\left(t_0\right),$$

where it is seen that the feedbacks, or cause and effect relations, consist of a state relation and a radiative sensitivity. Going further and assuming that ΔR and feedbacks are independent of t, and that the system actually makes it to equilibrium (i.e., $\Delta F \rightarrow 0$), (1.3) collapses to the classical expression (e.g., Schlesinger and Mitchell 1987)

$$\Delta T_s \approx \frac{-\Delta R}{\dfrac{\partial F}{\partial T_s}+\displaystyle\sum_i \frac{\partial F}{\partial x_i}\frac{\partial x_i}{\partial T_s}} \quad (1.4)$$

which upon expansion of F into its solar and terrestrial components yields the familiar form

$$\Delta T_s \approx \frac{-\Delta R}{\underbrace{\dfrac{\partial \mathcal{I}}{\partial T_s}+\dfrac{S_\odot}{4}\dfrac{\partial \alpha_p}{\partial T_s}}_{\text{initial}}+\displaystyle\sum_i \underbrace{\underbrace{\left[\frac{\partial \mathcal{I}}{\partial x_i}+\frac{S_\odot}{4}\frac{\partial \alpha_p}{\partial x_i}\right]}_{\substack{\text{radiative}\\ \text{sensitivities}}}\underbrace{\frac{\partial x_i}{\partial T_s}}_{\substack{\text{state}\\ \text{relations}}}}_{\text{feedbacks}}}. \quad (1.5)$$

The term labelled *initial* is also referred to as system gain. In the absence of feedbacks, it is the gain that brokers the response of T_s to ΔR. For example, doubling [CO_2] would increase Earth's atmospheric opacity and reduce net long-wave radiation at the tropopause resulting in $\Delta R \approx -4\,\mathrm{W\,m^{-2}}$ (Cess et al. 1993). Assuming that $T_s \approx 287\,\mathrm{K}$ and $\alpha_p \approx 0.3$, Earth's effective emissivity is

$$\varepsilon \approx \frac{\frac{S_\odot}{4}\left(1-\alpha_p\right)}{\sigma T_s^4} \approx 0.62, \quad (1.6)$$

and since changing $[CO_2]$ has a negligible impact on α_p,

$$\frac{\partial F}{\partial T_s} \approx \frac{\partial \mathcal{I}}{\partial T_s} \approx 4\varepsilon\sigma T_s^3 \approx 3.3\,\mathrm{W\,m^{-2}\,K^{-1}} \tag{1.7}$$

where σ is the Stefan–Boltzmann constant. Substituting these numbers into (1.4) implies that in the absence of feedbacks, doubling $[CO_2]$ would result in roughly $\Delta T_s \approx -\Delta R/4\varepsilon\sigma T_s^3 \approx 1.2$ K. The fact that GCM estimates of ΔT_s for doubling $[CO_2]$ range from $\sim$1 K to $\sim$5 K means that internal climatic variables work together to affect anything from a modest attenuation to a strong enhancement of the gain.

This attenuation and enhancement of system gain arises through feedbacks, or cause and effect relations, between internal variables. These relations are represented by the term in (1.5) labelled *feedbacks*. This is where almost all of the uncertainty about, and research into, climate prediction rests. Grouping feedback processes and gain together into a *global feedback parameter* as

$$\widehat{\Lambda} = \frac{\partial F}{\partial T_s} + \sum_i \frac{\partial F}{\partial x_i}\frac{\partial x_i}{\partial T_s} \tag{1.8}$$

and defining $\widehat{s} = -1/\widehat{\Lambda}$ as the *climate sensitivity parameter*, (1.4) becomes

$$\Delta T_s \approx \widehat{s}\Delta R. \tag{1.9}$$

This formulation is actually applicable to equilibria states only and there is no sound reason to believe that $\widehat{s}$ (or $\widehat{\Lambda}$) is independent of regime or time. Hence the motivation behind Aires and Rossow's (2003) formalism: $\widehat{s}$ depends on climatic state and simply boiling down a GCM simulation to one number is certainly an oversimplification, and at worst misleading.

Nevertheless, it has been proposed (e.g., Gregory et al. 2004; Stowasser et al. 2006) that useful information can be obtained by studying the phase trajectory of a perturbed model's recovery of radiative equilibrium. Begin by defining $\langle R'(t)\rangle$ as a model's time-dependent radiative imbalance at the TOA, where the initial perturbation is $\langle R'(0)\rangle = \Delta R$ and $\langle R'(\infty)\rangle = 0$, and $\langle T_s'(t)\rangle$ as a model's time-dependent change in mean surface temperature, where initially $\langle T_s'(0)\rangle = 0$ and equilibrium temperature change is $\langle T_s'(\infty)\rangle$. Then, plotting $\langle R'(t)\rangle$ vs. $\langle T_s'(t)\rangle$, one often finds that for long stretches of time, following an adjustment period where the GCM recovers from the shock of having ΔR administered to it suddenly,

$$\langle R'(t)\rangle \approx a + b\,\langle T_s'(t)\rangle \tag{1.10}$$

is a fair approximation in which $b = \widehat{\Lambda}$. In general, however, one could fit the results with some curvilinear function and analyze

$$\frac{\partial\,\langle T_s'\rangle}{\partial\,\langle R'\rangle} = -\widehat{s}(t)\,. \tag{1.11}$$

As discussed by Aires and Rossow and Barker and Räisänen (2005), isolating individual feedback relations and obtaining an estimate of $\widehat{\Lambda}$ from observations is a daunting task relative to studying only radiative sensitivities (i.e., $\partial F/\partial x_i$). Once one has profiles of information such as cloud fraction, mean water paths, variance of water paths, they can, however, be varied thereby estimating radiative sensitivities numerically. This goes for both model data and data inferred from observations that provide vertical profiles and horizontal transects of cloud properties (such as, for example, profiles obtained from the Atmospheric Radiation Measurement (ARM) Program's surface sites and active/passive satellite systems such as the A-train and EarthCARE).

In addition to sensitivities, radiative uncertainties can be defined as

$$\Delta F_{x_i} \approx \frac{\partial F}{\partial x_i} \Delta x_i \,, \tag{1.12}$$

where Δx_i is uncertainty for an internal variable x_i. Given a reasonable estimate of Δx_i, study of radiative uncertainties could help guide the extent to which effort should be expended on developing subgrid-scale parametrizations of radiative properties. For instance, if one is parametrizing x_i, yet it turns out that $\partial F/\partial x_i$, and ultimately ΔF_{x_i}, is very small for a realistic Δx_i, a parametrization as simple as a judicious global setting, as opposed to a detailed parametrization, that could be years in the making, may be sufficient.

The purpose of this discussion on climate sensitivities and analyses is to point out the central role of radiation and radiative transfer in both the climate system and models that attempt to capture some of its characteristics. In light of this, it is interesting to note that radiative transfer model intercomparison studies reported by Fouquart et al. (1991) and Barker et al. (2003) indicate that when several different radiative transfer models act on identical clear and cloudy atmospheres, the range of responses can be surprisingly large. Thus, it is still unclear how much of the disparity among GCM feedback parameters is due to different treatments of clouds, their optical properties, and different treatments of radiative transfer (particularly for cloudy atmospheres). Similarly, Collins (pers. comm., 2005) show that the much more straightforward radiative forcings due to changes in trace gas concentrations are still in question. This leads to GCM differences right off the top as *standardized* forcings used in GCM intercomparisons differ.

To summarize, representation of radiative transfer is crucial for confident prediction of climate and assessment of climate models. As such, the following sections discuss some current issues facing modelling of solar radiation in climate models.

1.3 Solar radiative transfer for global models

For reasons of tractability and justifiability in the face of numerous assumptions and uncertainties, essentially all global models employ two-stream approximations to solve for atmospheric radiative transfer. Since it appears that this will be the case for some time to come, barring the occasional jump to more sophisticated models (e.g., Gu and Liou 2001), this section gives a brief account of two-stream approximations for plane-parallel, homogeneous conditions, methods for extending two-streams, and finally solar transfer for Earth surfaces.

1.3.1 The Independent Column Approximation (ICA)

If one is provided with a surface–atmosphere domain $\mathcal{D}$ whose light attenuation properties can be described in three dimensions, domain-average albedo $\langle R \rangle$ (or transmittance, or flux in general) can be computed with an *exact* solution of the radiative transfer equation such that

$$\langle R \rangle = \iint_{\mathcal{D}} R_{\mathrm{3D}}\,(x,y)\;\mathrm{d}x\,\mathrm{d}y \Big/ \iint_{\mathcal{D}} \mathrm{d}x\,\mathrm{d}y\,, \tag{1.13}$$

where R_{3D} is albedo from a solution that accounts for the 3D flow of radiation. Now divide $\mathcal{D}$ into subcolumns and assume that radiation flows through each subcolumn independently of all other subcolumns, regardless of the cross-sectional area of the subcolumns, and that flow through each subcolumn can be described by 1D transport theory. This is the independent column approximation (ICA) of (1.13) which can be expressed as

$$\langle R \rangle = \iint_{\mathcal{D}} R_{\mathrm{1D}}\,(x,y)\;\mathrm{d}x\,\mathrm{d}y \Big/ \iint_{\mathcal{D}} \mathrm{d}x\,\mathrm{d}y\,, \tag{1.14}$$

where R_{1D} is from a 1D radiative transfer model that can range from a two-stream approximation to a Monte Carlo algorithm. Alternatively, (1.14) can be expressed as

$$\langle R \rangle = \sum_{n=1}^{\mathcal{N}} a(n) R_{\mathrm{1D}}\,(n) \Big/ \sum_{n=1}^{\mathcal{N}} a(n)\,, \tag{1.15}$$

where $\mathcal{D}$ is now recognized as consisting of $\mathcal{N}$ subcolumns of cross-sectional area $a(n)$. In most cases, a are equal for all n, and so (1.15) becomes simply

$$\langle R \rangle = \frac{1}{\mathcal{N}} \sum_{n=1}^{\mathcal{N}} R_{\mathrm{1D}}\,(n)\ . \tag{1.16}$$

On several occasions the ICA has performed very well for many different cloud regimes (Cahalan et al. 1994; Chambers et al. 1997; Barker et al. 1999; Benner and Evans 2001). Where (1.13) and (1.14) differ most is for large solar zenith angles θ_0 when energy input is small. The ICA tends to become an increasingly better approximation of (1.13) as $\mathcal{D}$ increases in size and temporal integration lengthens (Benner and Evans 2001). Thus, the ICA seems to be a reasonable standard for less rigorous models to aim for, especially when descriptions of the multi-point statistics of $\mathcal{D}$ are uncertain or unknown.

For GCMs, the cross-sectional area of $\mathcal{D}$ generally exceeds 10^4 km^2. Moreover, descriptions of unresolved fluctuations in optical properties inside $\mathcal{D}$ are, almost by definition, lacking. Hence, GCMs can justify using only 1D radiative transfer models within the ICA framework. The current paradigm is to apply

1D codes based on the two-stream approximation in which unresolved variability is either reduced to fractional coverage of homogeneous clouds that overlap according to extremely idealized configurations or incorporated directly into 1D transport solvers. Thus, the following subsections review two-stream approximations, their limitations, and some of the more popular attempts to extend their use in conjunction with the ICA.

1.3.2 Fluxes for single layers: the two-stream approximation

The steady-state, elastic radiative transfer equation can be written as

$$\boldsymbol{\Omega} \cdot \nabla I(\mathbf{x}, \boldsymbol{\Omega}) = \sigma(\mathbf{x}) I(\mathbf{x}, \boldsymbol{\Omega}) - \sigma_s(\mathbf{x}) \int p(\boldsymbol{\Omega} \cdot \boldsymbol{\Omega}') I(\mathbf{x}, \boldsymbol{\Omega}') \,\mathrm{d}\boldsymbol{\Omega}' - f(\mathbf{x}, \boldsymbol{\Omega}) \quad (1.17)$$

where $\mathbf{x}$ is position, $\boldsymbol{\Omega}$ is direction, I is radiance, σ is extinction coefficient, σ_s is scattering coefficient, p is scattering phase function describing the probability of radiation incident from direction $\boldsymbol{\Omega}$ being scattered into direction $\boldsymbol{\Omega}'$, and f is the attenuated source term. Exact solution of this equation for a general medium requires both much information regarding the nature of the medium and much computational power. Therefore, approximations are required for global models with the basic requirement being computation of reflectance and transmittance for individual model layers.

First, it is assumed that

$$\frac{\partial \begin{smallmatrix}\text{optical}\\ \text{properties}\end{smallmatrix}}{\partial x} = \frac{\partial \begin{smallmatrix}\text{optical}\\ \text{properties}\end{smallmatrix}}{\partial y} = \frac{\partial I}{\partial x} = \frac{\partial I}{\partial y} = 0\,. \quad (1.18)$$

which eliminates horizontal fluctuations in the atmosphere, surface, and radiation field. This simplifies (1.17) to the azimuthally-averaged 1D equation of transfer that can be written as

$$\begin{aligned} \mu \frac{\mathrm{d}I(\tau,\mu)}{\mathrm{d}\tau} &= I(\tau,\mu) - \frac{\omega_0}{2} \int_{-1}^{1} p(\mu;\mu') I(\tau,\mu') \,\mathrm{d}\mu' \\ &\quad - \frac{F_0}{4} \omega_0 p(\mu;\mu_0) \,\mathrm{e}^{-\tau/\mu_0}\,, \end{aligned} \quad (1.19)$$

where all terms have been azimuthally-averaged, F_0 is incoming solar at the top of atmosphere (TOA), μ is cosine of zenith angle, $\mu_0 = \cos\theta_0$, and

$$\mathrm{d}\tau = \sigma \,\mathrm{d}s; \qquad \omega_0 = \sigma_s/\sigma\,, \quad (1.20)$$

where s is geometric distance, τ is optical thickness, and ω_0 is single scattering albedo. Defining

$$F^{\pm}(\tau,\mu_0) = \int_0^1 \mu I(\tau, \pm\mu) \,\mathrm{d}\mu \quad (1.21)$$

as upwelling and downwelling irradiances, and applying the operators $\int_0^1 I(\tau,\mu)\,\mathrm{d}\mu$ and $\int_{-1}^0 I(\tau,\mu)\,\mathrm{d}\mu$ to (1.19) yields the coupled equations

$$\begin{cases} \dfrac{\mathrm{d}F^{+}(\tau,\mu_0)}{\mathrm{d}\tau} & = \gamma_1 F^{+}(\tau,\mu_0) - \gamma_2 F^{-}(\tau,\mu_0) - \dfrac{F_0}{4}\omega_0\gamma_3\,\mathrm{e}^{-\tau/\mu_0} \\ \dfrac{\mathrm{d}F^{-}(\tau,\mu_0)}{\mathrm{d}\tau} & = \gamma_2 F^{+}(\tau,\mu_0) - \gamma_1 F^{-}(\tau,\mu_0) + \dfrac{F_0}{4}\omega_0\gamma_4\,\mathrm{e}^{-\tau/\mu_0} \end{cases} \tag{1.22}$$

that can be solved readily by standard methods subject to specific boundary conditions where the coefficients $\gamma_1, \ldots,\ \gamma_4$ depend on assumptions made about I and p, as well as on μ_0 and optical properties. The general two-stream solution to (1.22) that describes layer reflectance and transmittance for absorbing layers irradiated by a collimated-beam from above with no upwelling or downwelling diffuse irradiances on the boundaries (Meador and Weaver 1980) is

$$R_{\mathrm{pp}}(\tau) = \frac{\omega_0}{\alpha}\frac{r_{+}\,\mathrm{e}^{k\tau} - r_{-}\,\mathrm{e}^{-k\tau} - r\,\mathrm{e}^{-\tau/\mu_0}}{\mathrm{e}^{k\tau} - \beta\,\mathrm{e}^{-k\tau}} \tag{1.23}$$

and

$$T_{\mathrm{pp}}(\tau) = \mathrm{e}^{-\tau/\mu_0}\left\{1 - \frac{\omega_0}{\alpha}\frac{t_{+}\,\mathrm{e}^{k\tau} - t_{-}\,\mathrm{e}^{-k\tau} - t\,\mathrm{e}^{-\tau/\mu_0}}{\mathrm{e}^{k\tau} - \beta\,\mathrm{e}^{-k\tau}}\right\}, \tag{1.24}$$

where

$$r_{\pm} = (1 \mp k\mu_0)\,(\gamma_1\gamma_3 - \gamma_2\gamma_4 \pm k\gamma_3)\ ;\ r = 2k\,[\gamma_3 - (\gamma_1\gamma_3 - \gamma_2\gamma_4)\,\mu_0]\,,$$

$$t_{\pm} = (1 \pm k\mu_0)\,(\gamma_1\gamma_4 - \gamma_2\gamma_3 \pm k\gamma_4)\ ;\ t = 2k\,[\gamma_4 - (\gamma_1\gamma_4 - \gamma_2\gamma_3)\,\mu_0]\,,$$

$$\alpha = \left[1 - (k\mu_0)^2\right](k + \gamma_1)\ ;\ k = \sqrt{\gamma_1^2 - \gamma_2^2}\,;\ \beta = -\frac{k - \gamma_1}{k + \gamma_1}\,.$$

Corresponding solutions when only isotropic diffuse irradiance is incident from above are

$$r_{\mathrm{pp}}(\tau) = \frac{\gamma_2(1 - \mathrm{e}^{-2k\tau})}{k + \gamma_1 + (k - \gamma_2)\,\mathrm{e}^{-2k\tau}} \tag{1.25}$$

and

$$t_{\mathrm{pp}}(\tau) = \frac{2k\,\mathrm{e}^{-k\tau}}{k + \gamma_1 + (k - \gamma_2)\,\mathrm{e}^{-2k\tau}}\,. \tag{1.26}$$

It can be verified that there is a removable singularity in (1.23) and (1.24) as $\omega_0 \to 1$. Thus, a separate solution to (1.22) for conservative scattering, $\omega_0 = 1$, has to be obtained which for collimated irradiance leads to (see Meador and Weaver 1980)

$$R_{\mathrm{pp}}(\tau) = \frac{\gamma_1\tau + (\gamma_3 - \gamma_1\mu_0)\left(1 - e^{-\tau/\mu_0}\right)}{1 + \gamma_1\tau} = 1 - T_{\mathrm{pp}}(\tau)\,, \tag{1.27}$$

while for diffuse irradiance

$$r_{\mathrm{pp}}(\tau) = \frac{\gamma_1\tau}{k + \gamma_1} = 1 - t_{\mathrm{pp}}(\tau)\,. \tag{1.28}$$

Numerous two-stream approximations can be defined depending on assumptions made about the nature of phase functions and the scattered radiance field (see Meador and Weaver 1980; Zdunkowski et al. 1980; King and Harshvardhan 1986; Appendix of this chapter). Over the past two decades, however, the approximation of choice among modelling groups has been delta-two-stream approximations. For these approximations, p is expressed as a combination of a smoothly varying portion and a sharp forward scattering peak:

$$p_\delta(\mu,\mu') \equiv 2g^2\delta(\mu - \mu') + \left(1 - g^2\right)\left(1 + \frac{3g\mu\mu'}{1+g}\right) , \tag{1.29}$$

where

$$g = \frac{1}{2}\int_{-1}^{1} \mu' p(\mu;\mu')\,\mathrm{d}\mu' \tag{1.30}$$

is asymmetry parameter, and δ is the Dirac distribution (Joseph et al. 1976). Figure 1.1 shows that for cloud droplets this approximation is good. It is straightforward to show that when this transformation is applied, all of the above presented equations are recovered, but layer optical properties are scaled as

$$\begin{aligned} \tau' &= (1 - \omega_0 g^2)\tau \\ \omega_0' &= \frac{(1-g^2)\omega_0}{(1-\omega_0 g^2)} \\ g' &= \frac{g}{1+g} . \end{aligned} \tag{1.31}$$

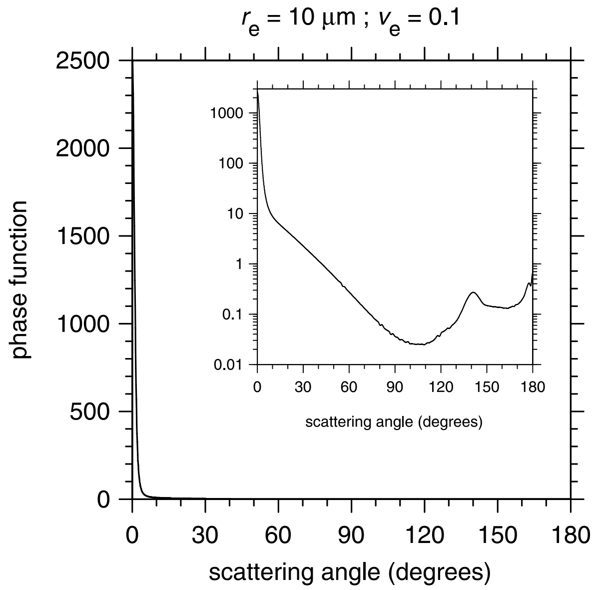

Fig. 1.1. Inset plot shows a log plot of the Mie scattering phase function as a function of scattering angle for a droplet size distribution with effective radius of 10 µm and effective variance of 0.1 at wavelength 0.6 µm. This is the usual way these functions are presented. The outer plot is the same as the inner except it is on a linear scale. Shown this way it is immediately apparent that the *delta* approximation in (1.29) is perfectly adequate for cloud droplets.

Delta-two-streams generally perform well for energetically-important high Sun conditions, but they scatter too little in near-forward directions and so for low Sun conditions they yield systematic underestimates of cloud and aerosol albedo. This is illustrated in Fig. 1.2 and may be of some concern in polar regions where during summer μ_0 is always small yet solar input is large (given long Sun-up periods). This deficiency in delta-two-streams can be largely rectified by shifting to the more computationally demanding delta-four-stream approximation (e.g., Li and Ramaswamy 1996).

Twenty years ago, King and Harshvardhan (1986) concluded that because of the assumptions upon which two-streams are based, no single two-stream approximation performs well under all conditions all the time. While this is still true today, (delta-) two-streams are unlikely, however, to be replaced, by another analytic model, as the model of choice in global models. This is because they are computationally inexpensive and given the crude cloud properties they operate on, it makes little sense to replace them with more sophisticated models such as, for example, four-streams or diffusion approximations.

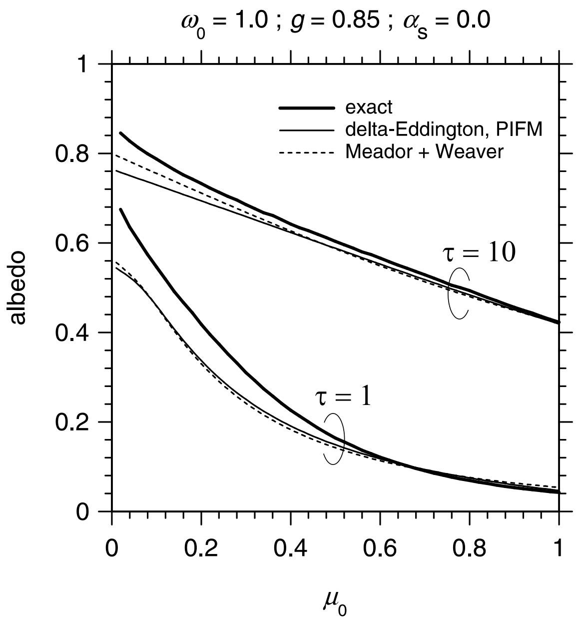

Fig. 1.2. Albedos for single layer, conservative scattering, homogeneous clouds (two optical depths as listed on the plot) as functions of cosine of solar zenith angle μ_0 using $g = 0.85$ and a black underlying surface. Heavy solid lines are *exact* solutions computed by DISORT (Stamnes et al. 1988), and other lines are two-stream approximations as listed. Note that for $\omega_0 = 1$, the delta-Eddington and Practical Improved Flux Method (PIFM) (Zdunkowski et al. 1980) are equivalent.

1.3.3 Linking layers

With reflectances and transmittances for individual layers in hand, they must be linked vertically in order to provide what global models are really after: heating rate profiles and surface absorption. This is achieved best with adding methods. For a simple two-layer system, total reflectance and transmittance are defined as

$$R_{1,2}(\mu_0) = R_1(\mu_0) + \frac{t_1\left\{\left[T_1(\mu_0) - T_1^{\mathrm{dir}}\right] r_2 + T_1^{\mathrm{dir}} R_2(\mu_0)\right\}}{1 - r_1 r_2} \tag{1.32}$$

and

$$T_{1,2}(\mu_0) = T_1^{\mathrm{dir}} T_2(\mu_0) + \frac{t_2\left\{\left[T_1(\mu_0) - T_1^{\mathrm{dir}}\right] + T_1^{\mathrm{dir}} R_2(\mu_0) r_1\right\}}{1 - r_1 r_2}\,, \tag{1.33}$$

where $T(\mu_0)$ and $R(\mu_0)$ are equivalent to T_{pp} and R_{pp} as derived above,

$$T_1^{\mathrm{dir}} = \mathrm{e}^{-\tau_1/\mu_0}\,, \tag{1.34}$$

and t and r are layer transmittances and reflectances for isotropic diffuse irradiance (see Liou 1992). The terms in these equations are portrayed schematically in Fig. 1.3. Note that the geometric sum formula has been applied under the assumption that internal reflectances and transmittances are all equal for all reflections. This is not the case for inhomogeneous media (see Barker and Davies 1992).

The expressions in (1.32) and (1.33) can be generalized to N number of layers. Flux profiles are then constructed by working up and down through the atmosphere computing reflectances and transmittances for collections of layers using

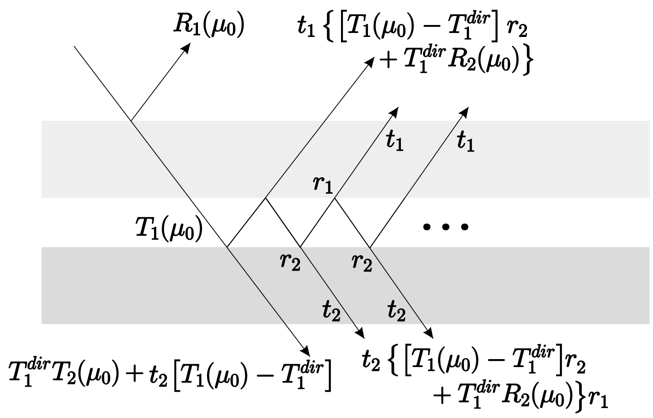

Fig. 1.3. Schematic showing how layers are linked in a SW adding scheme.

$$
\begin{aligned}
F_i^{\uparrow} &= \mu_0 S \left\{ \frac{T_{1,i-1}^{\mathrm{dir}} R_{i,N}(\mu_0) + \left[T_{1,i-1}(\mu_0) - T_{1,i-1}^{\mathrm{dir}} \right] r_{i,N}}{1 - r_{i-1,1} r_{i,N}} \right\} \\
F_i^{\downarrow} &= \mu_0 S \left\{ T_{1,i-1}^{\mathrm{dir}} + \frac{T_{1,i-1}^{\mathrm{dir}} R_{i,N}(\mu_0) r_{1,i-1} + \left[T_{1,i-1}(\mu_0) - T_{1,i-1}^{\mathrm{dir}} \right]}{1 - r_{i-1,1} r_{i,N}} \right\} ,
\end{aligned}
\tag{1.35}
$$

where double-subscripted diffuse reflectances represent values for collections of layers as indicated by the subscripts, and

$$
T_{1,i-1}^{\mathrm{dir}} = \exp\left[\sum_{k=1}^{i-1} \tau_k / \mu_0 \right] . \tag{1.36}
$$

Expressions like (1.35) can be computed for both clear and cloudy portions of an atmosphere. Layers can then be linked depending on the desired nature of vertical overlap of cloud. The most common way to proceed is to assume that clouds in adjacent layers are maximally overlapped and that collections of layers containing contiguous clouds that are separated by cloudless layers are randomly overlapped (e.g., Geleyn and Hollingsworth 1979). This approach has become the paradigm despite it being an extreme approximation that depends on model vertical resolution, and systematically underestimating total cloud fraction and atmospheric reflectance (see Barker et al. 2003).

1.3.4 When is the two-stream approximation applicable?

As mentioned at the beginning of the previous section, the heart of two-stream approximations is the assumption that the medium and boundary conditions are uniform. Since this applies to individual layers, vertical inhomogeneity is not an issue, at least when layers are homogeneous slabs, as the atmosphere can be partitioned vertically into as many homogeneous layers as one sees fit (Wiscombe 1977). Likewise, it is usually appropriate to use two-stream approximations for computation of flux profiles for cloudless atmospheres. This is because horizontal variations in air density across regions the size of GCM cells are typically very small, and hence so too are variations in scattering efficiencies. Moreover, variations in absorbing gases are generally of second-order importance too, and so use of mean mixing ratios to compute extinction coefficients, and optical depths, are appropriate. The same goes for aerosols in cloudless atmospheres as their concentrations are generally in the linear-response regime for reflectance and transmittance. If the underlying surface albedo is inhomogeneous, simple linear averaging of albedo and using the result in a two-stream approximation will lead to errors (see Barker 2005), but again, these errors are most often second-order.

Where standard two-streams do encounter serious troubles, however, are with realistic cloudy atmospheres. This is because most portions of cloudy atmospheres that span domains the size of typical GCM cells are horizontally inhomogeneous with fluctuations that often bridge the nonlinear response regime for reflectance and transmittance. As such, assumptions upon which two-streams are based are often seriously violated. Since these are extreme assumptions, one can expect systematic errors which are the most offensive errors for a dynamical model as they manifest themselves as *phantom* forcings. That is, their presence goes undetected because while the two-stream itself might be working perfectly, the dynamical model may demonstrate unreasonable behaviour that could prompt adjustments to be made to unrelated parameters. To make matters worse, clouds are neither totally uncorrelated nor perfectly correlated in the vertical and this confounds attempts to vertically link horizontally inhomogeneous cloudy layers. Furthermore, the layers that a GCM is partitioned into are, for all intents and purposes, arbitrary and so cloud layers in a GCM are not layered clouds that get reported by observers.

Regarding horizontal fluctuations, the bias resulting from use of a regular two-stream can be demonstrated easily. Figure 1.4 shows albedo for two values of optical depth τ_1 and τ_2. If these values occur with equal probability, mean optical depth is simply $(\tau_1 + \tau_2)/2$. If one operates on this mean value with the two-stream one gets an albedo that is sytematicaly greater than the result obtained by operating on each value separately and averaging the responses. This off-set is known as the *homogeneous bias*. It can be stated generally by Jensen's integral inequality (Gradshteyn and Ryzhik 1980) as

$$\int_0^\infty p(\tau)R_{\mathrm{pp}}(\tau)\,\mathrm{d}\tau \leqslant R_{\mathrm{pp}}\left(\int_0^\infty \tau p(\tau)\,\mathrm{d}\tau\right) = R_{\mathrm{pp}}(\overline{\tau})\,. \tag{1.37}$$

For transmittance the inequality is reversed because the concavity of the response function is opposite that for reflectance.

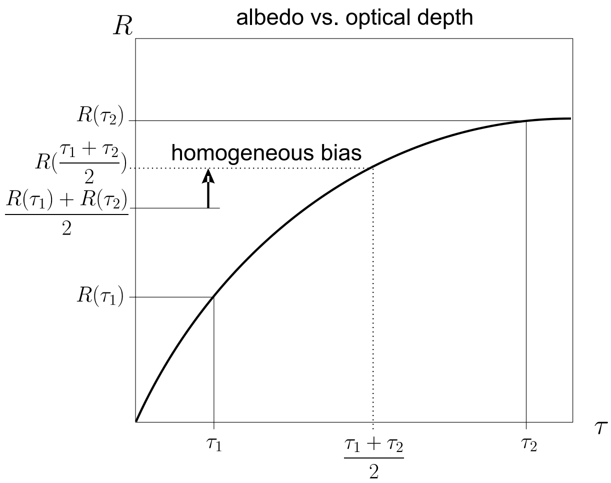

Fig. 1.4. Schematic showing albedo R for a plane-parallel, homogeneous cloud layer as a function of optical depth τ. Two equally likely values τ_1 and τ_2 yield responses $R(\tau_1)$ and $R(\tau_2)$ which when averaged produce a mean albedo that is less than that obtained by R operating on mean optical depth $(\tau_1 + \tau_2)/2$.

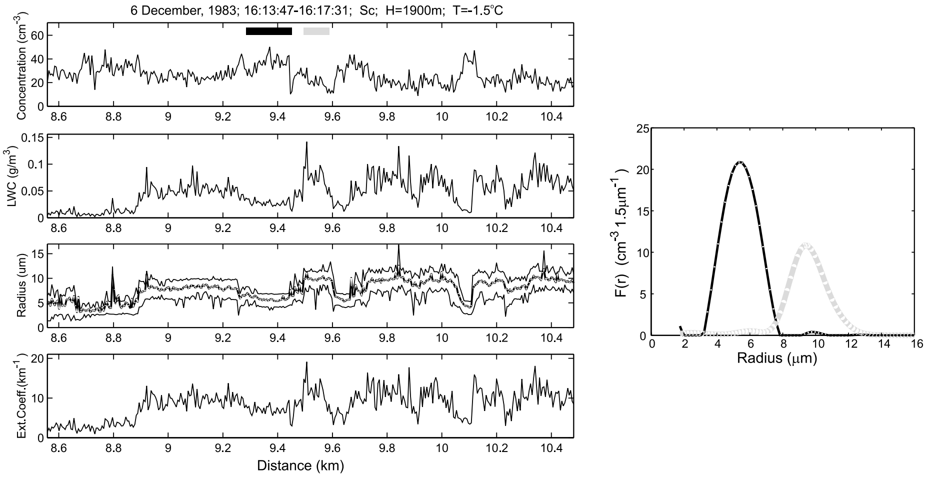

Fig. 1.5. Plot in the upper left shows concentration of cloud droplets recorded by an aircraft flying 1900 m above the former Soviet Union on Dec. 6, 1983. Plots beneath this one show cloud liquid water content (LWC), droplet effective radius, and extinction coefficient. Plot on the right shows the droplet size distributions for two sections of the flight as shade-coded on the plot in the upper left. (Data courtesy of A. Korolev, 2002.)

Figure 1.5 shows an example of data collected along a 2.5 km level transect by an instrumented aircraft. It shows that cloud droplet concentration, liquid water content, droplet size distribution, and hence extinction coefficient all vary at all scales. Since situations like this have be expected to occur at unresolved scales in GCMs, it is clear that the homogeneous assumption is untenable (cf. Clothiaux et al. 2005).

Demonstrating limitations of two-streams, or plane-parallel models in general, to vertical overlap of fractional cloud is not as simple. The most common assumption made in GCMs is that when clouds are separated by a cloudless layer they are randomly overlapped, and that when they are in contiguous layers they are maximally overlapped. The latter condition can be confusing. Take for example the three layer system shown in Fig. 1.6 with layer cloud amounts A_i. The top left shows true maximal overlap for contiguous clouds. Here there are three possible combinations of total cloud optical depth. The top right shows what happens when one adheres to the maximum-random overlap rule where cloud common to all three layers are maximally overlapped but the overhanging portions in layers 1 and 3 are randomly overlapped. Now there are four combinations of total cloud optical depth. Clearly these scenarios have different total cloud fractions and distributions of vertically integrated optical depth, and so their radiative responses will differ too (see Barker et al. 1999).

In general, however, there is no reason to assume that clouds cut into arbitrary layers, as they are in a GCM, will abide by the vertical resolution-dependent maximum-random overlap rule, whatever one's interpretation of it might be. Rather, one can expect something more general like that shown in the

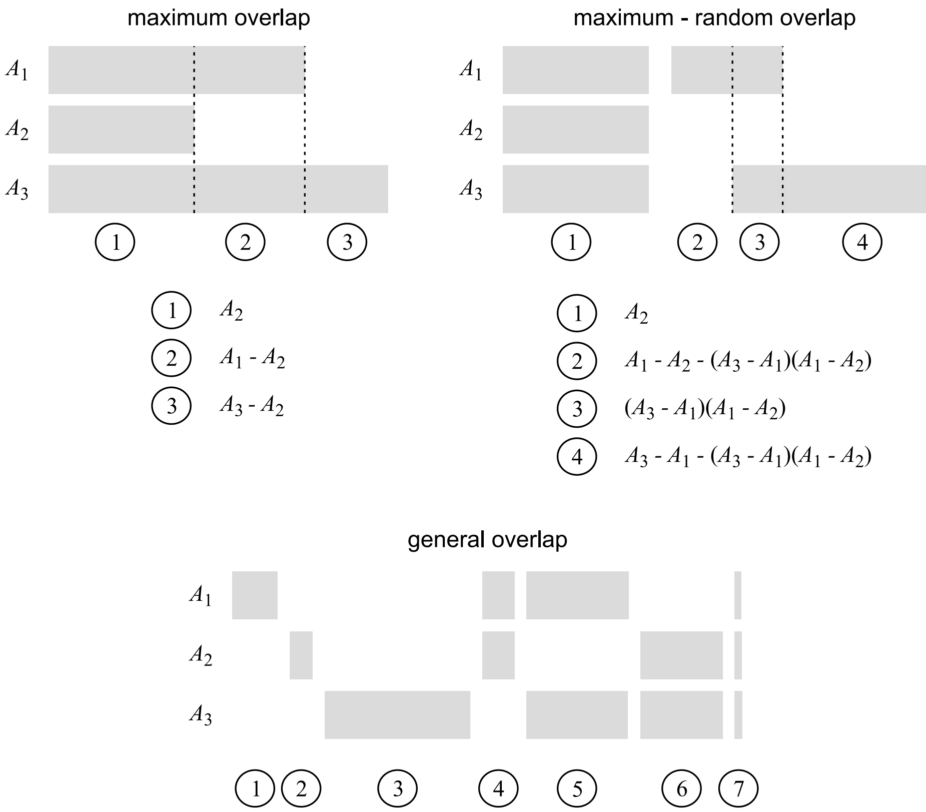

Fig. 1.6. Schematic in the upper left shows three contiguous layers of cloud in maximum overlap configuration. Cloud fractions are A_1, A_2, and A_3. Fractional amounts for the three distinct vertical integrals are listed beneath the schematic. The schematic in the upper right shows the same layer cloud fractions in maximum-random overlap mode. Lower schematic shows an example of the same clouds overlapping in a general manner where all seven possible vertical combinations of cloud are realized.

lower part of Fig. 1.6. While this might not differ much from maximum overlap if the three layers are thin, one can expect large differences when there are many more than three layers that extend over a significant fraction of the lower atmosphere; such as with towering convective clouds where a spectrum of clouds in various stages of life can be expected to occur for domains the size of GCM cells (e.g., Hogan and Illingworth 2000; Mace and Benson-Troth 2002; Stephens et al. 2004).

1.3.5 Strategies to extend two-stream approximations

Again, because the two-stream is reasonably accurate and computationally very efficient, several attempts have been made to extend its range of application to include horizontally inhomogeneous clouds and various vertical overlap assumptions. In this section, the most popular methods, all of which have been used in GCMs, are reviewed and critiqued.

All of these methods are based on the assumption that domain-average reflectance (or transmittance, absorptance, or flux in general) can be computed as

$$\langle R \rangle = (1 - A_{\mathrm{c}}) \langle R_{\mathrm{clr}} \rangle + A_c \langle R_{\mathrm{cld}} \rangle \ , \tag{1.38}$$

where A_{c} is layer cloud fraction, and $\langle R_{\mathrm{clr}} \rangle$ and $\langle R_{\mathrm{cld}} \rangle$ are mean reflectances associated with the clear and cloudy portions of the layer, respectively. The basic idea here is that radiation that interacts with the cloudy portion of a layer does not interact with the clear portion, and vice versa (cf. Stephens 1988). In this sense, (1.38) is fundamentally an ICA. Moreover, (1.38) relies completely on the concept of cloud fraction which is often discussed and presented in passing without question or hesitation yet as soon as one attempts to describe it with any formality, one recognizes that it is fraught with confusion and misinterpretation. The only reason we passively accept it in (1.38) is because we are approaching the problem with a plane-parallel vision of atmospheric layers and have computation of average fluxes for large domains in mind.

1.3.5.1 Gamma-weighted two-stream approximation (GWTSA)

This model is an example of an explicit independent column approximation (ICA). Its starting point is to rewrite the area integral in (1.14) in its distribution form as

$$\langle R_{\mathrm{cld}} \rangle = \int_0^\infty p\,(\tau)\, R_{\mathrm{1D}}\,(\tau)\ \mathrm{d}\tau\,, \tag{1.39}$$

where $p\,(\tau)$ is a normalized density function that describes variations in τ over a domain (Ronnholm et al. 1980; Cahalan 1989; Stephens et al. 1991). There are several ways to solve (1.39) depending on the functional forms of $p\,(\tau)$ and $R_{\mathrm{1D}}\,(\tau)$. Clearly, if the forms are intractable and require numerical integration, (1.39) is not tenable for use in GCMs. Several studies (e.g., Barker et al. 1996) using satellite-inferred values of τ and cloud-resolving model data have shown that for domains the size of those used in typical GCMs it is reasonable to represent $p\,(\tau)$ by a gamma distribution defined as

$$p_\gamma\,(\tau) = \frac{1}{\Gamma(\nu)} \left(\frac{\nu}{\overline{\tau}}\right)^{\nu} \tau^{\nu-1}\, \mathrm{e}^{-\nu\tau/\overline{\tau}}\,, \tag{1.40}$$

where ν is related to the variance of τ, and $\Gamma(\nu)$ is the gamma function. Note that if particle size distribution is assumed to be constant, (1.40) applies to cloud water content and water path too.

By substituting the generalized, non-conservative scattering, two-stream approximation for collimated irradiance given by (1.23) and (1.24) along with (1.40) into (1.39) leads to the gamma-weighted two-stream approximation (GWTSA) (Barker 1996) in which

$$\langle R_{\mathrm{cld}} \rangle = \phi_1^\nu \frac{\omega_0}{\alpha} \left[r_+ \mathcal{F}\,(\beta,\nu,\phi_1) - r_- \mathcal{F}\,(\beta,\nu,\phi_2) - r \mathcal{F}\,(\beta,\nu,\phi_3) \right] \tag{1.41}$$

and

$$\langle T_{\text{cld}} \rangle = \left(\frac{\nu}{\nu + \overline{\tau}/\mu_0} \right)^{\nu} - \phi_1^{\nu} \frac{\omega_0}{\alpha} \left[t_+ \mathcal{F}(\beta, \nu, \phi_4) - t_- \mathcal{F}(\beta, \nu, \phi_5) - t \mathcal{F}(\beta, \nu, \phi_6) \right] \tag{1.42}$$

where

$$\mathcal{F}(\beta, \nu, \phi) = \sum_{n=0}^{\infty} \frac{\beta^n}{(\phi + n)^{\nu}} \ ; \ |\beta| \le 1, \ \beta \ne 1, \ \nu > 0,$$

which is known formally as the Lerch transcendent, and

$$\begin{aligned} \phi_1 &= \frac{\nu}{2k\overline{\tau}} &;\ \phi_4 &= \phi_1 + \frac{1}{2k\mu_0} \\ \phi_2 &= \phi_1 + 1 &;\ \phi_5 &= \phi_4 + 1 \\ \phi_3 &= \phi_4 + \frac{1}{2} &;\ \phi_6 &= \phi_1 + \frac{1}{2}. \end{aligned}$$

As $\omega_0 \to 1.0$, $\beta \to 1$ and one approaches the removable singularity in (1.41) and (1.42). Therefore, substituting (1.27) and (1.40) into (1.39) yields the conservative scattering GWTSA as

$$\begin{aligned} \langle T_{\text{cld}} \rangle &= \left(\frac{\nu}{\gamma_1 \overline{\tau}} \right)^{\nu} \left[(\gamma_1 \mu_0 + \gamma_4) \mathcal{G}\left(1 - \nu, \ \frac{\nu}{\gamma_1 \overline{\tau}} \right) \right. \\ &\qquad \left. - (\gamma_1 \mu_0 - \gamma_3) \mathcal{G}\left(1 - \nu, \ \frac{\nu \mu_0 + \overline{\tau}}{\gamma_1 \mu_0 \overline{\tau}} \right) \right] \\ &= 1 - \langle R_{cld} \rangle \end{aligned} \tag{1.43}$$

where

$$\mathcal{G}(1 - \nu, x) = \mathrm{e}^{x} \Gamma(1 - \nu, x) \, .$$

For diffuse irradiance, the non-conservative solutions are

$$\langle r_{\text{cld}} \rangle = \phi_1^{\nu} \frac{\gamma_2}{k + \gamma_1} \left[\mathcal{F}(\beta, \nu, \phi_1) - \mathcal{F}(\beta, \nu, \phi_2) \right] \tag{1.44}$$

and

$$\langle t_{\text{cld}} \rangle = \phi_1^{\nu} \frac{2k}{k + \gamma_1} \mathcal{F}(\beta, \nu, \phi_6) \, , \tag{1.45}$$

while the conservative scattering solution is (Oreopoulos and Barker 1999)

$$\langle r_{\text{cld}} \rangle = 1 - \left(\frac{\nu}{\gamma_1 \overline{\tau}} \right)^{\nu} \mathcal{G}\left(1 - \nu, \ \frac{\nu}{\gamma_1 \overline{\tau}} \right) = 1 - \langle t_{\text{cld}} \rangle \, . \tag{1.46}$$

Naturally, other solutions are possible for different representations of $p(\tau)$. For instance, if $p(\tau)$ is approximated by a beta distribution, one ends up with rather intractable solutions for $\langle R_{\text{cld}} \rangle$ and $\langle T_{\text{cld}} \rangle$ involving hypergeometric functions. A closed-form solution using a lognormal distribution for τ has not been found as yet. Likewise, it is not known whether closed-form solutions exist for a gamma-weighted four-stream.

To conclude, the attraction of this approach is that as long as one is willing to accept that the underlying distribution of τ can be represented by $p_\gamma(\tau)$, and that the ICA is a reasonable benchmark for GCM-style radiative transfer models to aim for, the GWTSA represents, by definition, an exact solution for single layers. The GWTSA, for both SW and LW radiation, is being used currently in the CCCma GCM (Li and Barker 2002; Li et al. 2005). It should be noted, however, that the GWTSA encounters problems when it comes to linking layers (see Oreopoulos and Barker 1999).

1.3.5.2 Effective thickness approximation (ETA)

Following from (1.37), an obvious approach to approximate $\langle R_{\mathrm{cld}} \rangle$ is

$$\langle R_{\mathrm{cld}} \rangle \approx R_{\mathrm{pp}} \left[f(\overline{\tau}) \right] ,$$

where $f(\overline{\tau}) \leqslant \overline{\tau}$ represents some transformation to $\overline{\tau}$. What makes this approach desirable is that it utilizes directly the efficient two-stream solution with, ideally, only a minor adjustment to its input.

Davis et al. (1990) hypothesized that $\langle R_{\mathrm{cld}} \rangle$ could be approximated as

$$\langle R_{\mathrm{cld}} \rangle \approx R_{\mathrm{pp}}(\overline{\tau}^{\delta}) , \tag{1.47}$$

where δ was referred to as a co-packing factor. The authors determined δ from Monte Carlo simulations for very heterogeneous fractal cloud models based on singular cascades. This parametrization found its way into at least one operational GCM (McFarlane et al. 1992). In general $\delta \leq 1$, but for $\overline{\tau} < 1$ δ has to exceed 1 or its purpose is defeated. This produces the desired effect by reducing the value of $R_{\mathrm{pp}}(\overline{\tau})$, but given its simplicity and high level of parametrization, results can be expected to be, at best, very approximate.

Cahalan et al. (1994) advanced the potential applicability of the ETA, in principle for stratocumulus layers only, by noting that expansion of R_{pp} in a Taylor series about $\overline{\log_{10} \tau}$ and averaging over all cells of a bounded cascade model yields

$$\langle R_{\mathrm{cld}} \rangle = R_{\mathrm{pp}} \left(\eta \overline{\tau} \right) + \sum_{n=1}^{\infty} M_{2n} \frac{\partial^{2n} R_{\mathrm{pp}} \left(\eta \overline{\tau} \right)}{\partial \left(\log_{10} \tau \right)^{2n}} , \tag{1.48}$$

where M_{2n} is related to the $2n$th moment of $\log_{10} \tau$, and

$$\eta = \frac{e^{\overline{\ln \tau}}}{\overline{\tau}} \leqslant 1 \tag{1.49}$$

is the reduction factor. Cahalan et al. presented results for (1.48) in its simplest form of

$$\langle R_{\mathrm{cld}} \rangle \approx R_{\mathrm{pp}}(\eta \overline{\tau}). \tag{1.50}$$

Cahalan et al. (1994, 1995) estimated η to be roughly 0.6 to 0.7 for marine boundary layer clouds off the coast of California and on Porto Santo Island. These estimates were obtained by compositing several days' worth of 30 s or

1 min observations of cloud LWP inferred from microwave radiometer data. By compositing data, however, the PPH bias can be made arbitrarily large as more and more variability becomes unresolved and subsumed into η, or any other measure of variance. Hence, values of η that are arrived at by compositing several days of data are applicable to GCMs that call their ETA just once a day or so. Most GCMs call their radiation codes at least once per hour, so if they used values of η derived from compositing over extended periods, they would effectively double-count the impact of cloud variability. Subsequent analyses indicate that for most overcast marine boundary layer clouds, $\eta \approx 0.9$ (Barker et al. 1996; Pincus et al. 1999; Rossow et al. 2002). Nevertheless, (1.50) has been used in operational GCMs. For example, Tiedtke (1996) used $\eta \approx 0.7$ for all clouds all the time.

1.3.5.3 ETA vs. GWTSA and the assumption of underlying distributions for τ

Based on the previous paragraph, one might conclude, correctly, that there is still confusion regarding description of unresolved cloud structure in GCMs. This is compounded by the fact that GCMs require information on a per-layer basis, not for entire cloud fields as is often estimated from passive satellite imagery (e.g., Barker et al. 1996; Oreopoulos and Davies 1998). Moreover, even if one felt comfortable about setting values of ν and η, there is still the question: what is the underlying distribution of τ? In this subsection we explore the importance of this question.

Basically, there are two situations: a non-analytic representation for $p(\tau)$, or an assumed analytic form for $p(\tau)$. In either case, one could compute, at potentially great computational expense, the ICA solution using (1.16) or (1.39), respectively. On the other hand, it is easy to compute corresponding statistics such as $\overline{\tau}$, $\overline{\ln\tau}$, σ, ν, and η. Once computed, they can be used directly in either the ETA or the GWTSA. For the latter, one makes the explicit assumption that for computation of mean radiative fluxes, the gamma distribution is suitable regardless of what $p(\tau)$ the parameters come from. At the same time, the gamma distribution could also drive estimates of η to be used in the ETA.

For tractability, R_{pp} is represented here by Coakley and Chýlek's (1975) 'model 1' approximation for $\omega_0 = 1$ in which

$$R_{\mathrm{pp}}(\tau) = \frac{\beta(\mu_0)\tau}{\mu_0 + \beta(\mu_0)\tau} = 1 - T_{\mathrm{pp}}(\tau)\,, \tag{1.51}$$

where $\beta(\mu_0)$ is the zenith angle dependent backscatter function (Wiscombe and Grams 1976). When an analytic distribution for τ is used, it is assumed to be $p_\gamma(\tau)$. On the other hand, non-analytic distributions of τ are realized by the bounded cascade (BC) model of Cahalan et al. (1994). For the most part, the variability of τ for the BC model depends on the *fractal parameter* f_0 which is related to η and M_2 [see (1.48)] as

$$\eta = \sqrt{\prod_{n=0}^{\infty} (1 - f_0^2 c^{2n})}$$

and

$$M_2 = \sum_{n=1}^{\infty} \left[\frac{1}{2} \log \left(\frac{1 + f_0 c^n}{1 - f_0 c^n} \right) \right]^2 ,$$

where $c \in (0, 1]$ but is generally set to $2^{-1/3}$.

Consider first the distributions produced by the BC model. These distributions resemble lognormal distributions, and for $f_0 \lesssim 0.3$ they resemble gamma distributions too. It is most likely that for layers with dimensions resembling those found in GCMs $f_0 \in [0.2, 0.7]$. Figure 1.7 shows albedo as a function of f_0 for several models. ICA values were computed by (1.16) and differences between ICA and homogeneous are known as the homogeneous bias. The ETA proper is represented by (1.50) where η were computed directly from BC data using (1.49). For $\mu_0 = 0.5$ and $\overline{\tau} = 10$, this model does extremely well, but for $\mu_0 = 1$ it overestimates the homogeneous bias systematically. Inclusion of the second term in (1.48), with M_2 computed directly from data, improves estimates notably. For $\mu_0 = 1$, however, it still underestimates the ICA systematically.

At this point, assume that the underlying distribution of τ is $p_\gamma(\tau)$. It can be shown that (1.48) can be expressed as

$$\langle R_{\text{cld}} \rangle = R_{\text{pp}}(\eta\overline{\tau}) + \left[\frac{1}{2 \ln 10} \psi_1(\nu) \right] \frac{\partial^2 R_{\text{pp}}\,(\eta\overline{\tau})}{\partial (\ln \tau)^2} + \cdots , \tag{1.52}$$

where

$$\eta = \frac{e^{\psi_0(\nu)}}{\nu} , \tag{1.53}$$

and

$$\psi_n(\nu) = \frac{d^{n+1}}{d\nu^{n+1}} \ln \Gamma\,(\nu)$$

is the polygamma function. Although $\psi_n(\nu)$ are easy to parameterize, multiple derivatives of R_{pp} are tedious in general. Substituting (1.51) into (1.52) and retaining just the first two terms gives

$$\langle R_{\text{cld}} \rangle \approx R_{\text{pp}}(\eta\overline{\tau}) \left\{ 1 + \frac{\mu_0 \left[\mu_0 - \beta(\mu_0)\eta\overline{\tau} \right]}{2 \ln{(10)} \left[\mu_0 + \beta(\mu_0)\eta\overline{\tau} \right]^2} \psi_1(\nu) \right\} . \tag{1.54}$$

Even for (1.51) the third term is already too intractable to be of much use. Figure 1.7 shows that when only the leading term in (1.54) is used with η computed by (1.53) and ν by the method of moments (mom), which is defined as

$$\nu_{mom} = \left(\frac{\overline{\tau}}{\sigma} \right)^2 ,$$

where σ is standard deviation of τ, the situation worsens greatly. This is because ν_{mom} is impacted too much by extreme values of τ and so corresponding η are too small as are albedos.

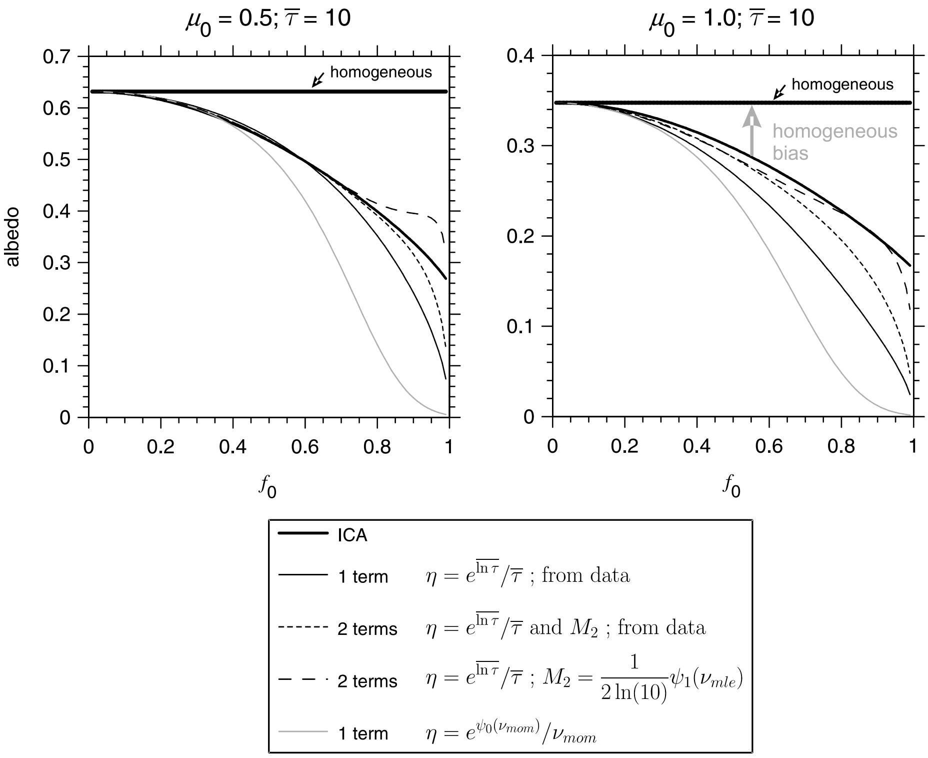

Fig. 1.7. Albedo for non-absorbing clouds as a function of the bounded cascade model's fractal parameter f_0 ($f_0 = 0$ homogeneous) for two solar zenith angles and $\overline{\tau} = 10$. See the text for a description of the various model results shown here.

The maximum likelihood estimate (MLE) of ν is

$$\psi_0(\nu_{mle}) + \ln\left(\frac{\overline{\tau}}{\nu_{mle}}\right) - \overline{\ln\tau} = 0, \tag{1.55}$$

which upon rearranging as

$$\frac{e^{\psi_0(\nu_{mle})}}{\nu_{mle}} = \frac{e^{\overline{\ln(\tau)}}}{\overline{\tau}}$$

verifies that explicit computation of η from data yields the same reduction factor as does use of the gamma distribution's MLE value for ν in (1.53). In general, ν_{mle} differs from ν_{mom}. Interestingly, Fig. 1.7 shows that when one uses η computed directly from data, or by (1.53) with ν_{mle}, in conjunction with the second term of (1.54), results generally improve over the use of two terms with parameters set directly from data (especially for $\mu_0 = 1$).

The other end of the spectrum is to assume that distributions of τ are in actuality gamma distributions. In this case $\nu_{mle} = \nu_{mom}$. Substituting (1.40)

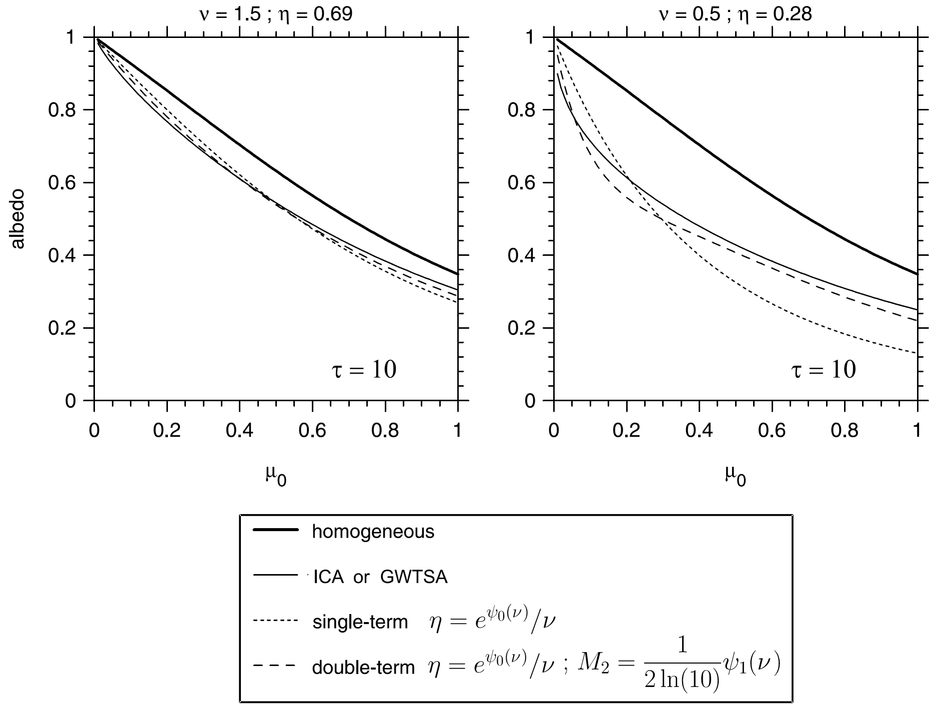

Fig. 1.8. Conservative scattering albedo of an overcast cloud layer with $\overline{\tau} = 10$ as a function of cosine of solar zenith angle μ_0. Results are shown for two inhomogeneous clouds with ν and η as listed at the top of each plot, as well as for their homogeneous counterpart which corresponds to $\nu \to \infty$ and $\eta = 1$.

and (1.51) into (1.39) and evaluating the integral yields

$$\langle R_{\mathrm{cld}} \rangle = 1 - e^{\xi + \nu \ln \xi} \Gamma\left(1 - \nu,\ \xi\right) = 1 - \langle T_{\mathrm{cld}} \rangle\ , \tag{1.56}$$

where

$$\xi = \frac{\nu \mu_0}{\beta(\mu_0)\overline{\tau}},$$

and $\Gamma(1 - \nu,\ \xi)$ is the incomplete gamma function. Equation (1.56) represents one of the simplest forms of the GWTSA. By definition, the GWTSA is now equivalent to the ICA and so, in this situation, produces perfect estimates of the homogeneous bias. Now the tables are turned and, as Fig. 1.8 shows, it is the single term ETA that produces poor estimates of albedo. In fact, it performs well only when $\eta\overline{\tau} \approx \mu_0/\beta(\mu_0)$ or when M_{2n} are small (i.e., variability is weak). Again, however, inclusion of the second term improves estimates significantly over those of the simple ETA.

1.3.5.4 Renormalization of optical properties

Cairns et al. (2000) developed an approximate solution that is based on assumptions similar to Stephens's (1988) method. First, they assume that the number concentration of scatters can be described by

$$n(\mathbf{x}) = \overline{n} + n'(\mathbf{x}) \tag{1.57}$$

where $\overline{n}$ is domain-average number concentration, n' is a local fluctuation at position $\mathbf{x}$, and that fluctuations are isotropic in three-dimensions. Averaging the 3D radiative transfer equation over the domain leads them to domain-average intensity $\overline{I(\mathbf{x}, \boldsymbol{\Omega})}$ given by

$$\begin{aligned} \boldsymbol{\Omega} \cdot \nabla\overline{I(\mathbf{x}, \boldsymbol{\Omega})} \ + \ \sigma\overline{n} \int_{4\pi} & B(\mathbf{x} \cdot \boldsymbol{\Omega}')\overline{I(\mathbf{x}, \boldsymbol{\Omega}')} \, \mathrm{d}\boldsymbol{\Omega}' \\ &= -\sigma \int_{4\pi} B(\boldsymbol{\Omega} \cdot \boldsymbol{\Omega}')\overline{n'(\mathbf{x})I(\mathbf{x}, \boldsymbol{\Omega}')} \, \mathrm{d}\boldsymbol{\Omega}' \, , \end{aligned} \tag{1.58}$$

where

$$B(\mathbf{s} \cdot \mathbf{s}') = \delta(\boldsymbol{\Omega} \cdot \boldsymbol{\Omega}' - 1) - \omega_0 p(\boldsymbol{\Omega} \cdot \boldsymbol{\Omega}'),$$

and $\boldsymbol{\Omega}$ is angular direction. In an attempt to close (1.58), Cairns et al. rewrite (1.58) as an integral equation involving a Green's function, perform a perturbation expansion, and re-sum the series. This effectively decouples the term $\overline{n'(\mathbf{x})I(\mathbf{x}, \boldsymbol{\Omega}')}$ in (1.58). They then invoke the nonlinear approximation, and assuming the effects of fluctuations are local (i.e., not long-range), they are able to recover the LHS of (1.58) which can be solved as though the medium was homogeneous with the following transformed domain-average optical properties:

$$\begin{aligned} \sigma' \ &= \ \sigma\,(1-\varepsilon) \ , \\ \omega_0' \ &= \ \omega_0 \left[1 - \frac{\varepsilon}{1-\varepsilon}\,(1-\omega_0)\right] \ , \\ \omega_0' g' \ &= \ \omega_0 g \left[1 - \frac{\varepsilon}{1-\varepsilon}\,(1-\omega_0 g)\right] \ , \end{aligned} \tag{1.59}$$

where

$$\varepsilon = \frac{1}{2}\left(q - \sqrt{q^2 - 4V}\right),$$

and

$$q = \frac{1 + \sigma l_c}{\sigma l_c} \, ,$$

where V is relative variance of n, and l_c is effective correlation length of the variations. When $\sigma l_c \approx 1$, particle density fluctuations follow a lognormal distribution. In this case, however, only moderate fluctuations are allowed (i.e., $V < 1$). For a more thorough assessment of this method, see Barker and Davis (2005).

From Cairns et al.'s (2000) initial formulation, it would appear that long-range fluctuations in $n(\mathbf{x})$ are neglected thereby rendering the transformations in (1.59) applicable on relatively small scales such as individual cells of a stratocumulus or individual cumuli. Cairns et al. allude to the ICA being more suitable at describing the effect of fluctuations larger than the mean diffusion length. Nevertheless, Rossow et al. (2002) applied (1.59) to ISCCP (International Satellite Cloud Climatology Project) data, which has a horizontal resolution of ∼5 km, and defined ε as

$$\varepsilon = 1 - \frac{\widehat{\tau}}{\overline{\tau}}\,, \tag{1.60}$$

where

$$\widehat{\tau} = R_{\mathrm{pp}}^{-1}\left[\frac{1}{N}\sum_{n=1}^{N} R_{1D}\left(\tau_n\right)\right]$$

in which N is the number of satellite pixels in a large domain, and τ_n is cloud optical depth inferred for the nth pixel. In the appendix to Rossow et al. (2002), it was shown that an accurate approximation relating ν_{mle} [see (1.55)] and ε is

$$\nu_{mle} = \frac{1}{\varepsilon - \ln\left(1-\varepsilon\right)}\,. \tag{1.61}$$

While Cairns et al.'s (2000) model does not suffer from the same ailment that Stephens's (1988) does (i.e., potential violation of the conservation of energy; see Barker and Davis 2005), it would appear from their initial presentation that it is meant to be applied at small scales; perhaps superimposed onto another model designed to account for fluctuations at larger scales, such as the GWTSA.

1.3.5.5 The Monte Carlo Independent Column Approximation (McICA)

Several studies have shown that differences in estimates of domain-averaged flux profiles predicted by the ICA and 3D radiative transfer models are usually small (Cahalan et al. 1994; Barker et al. 1999, 2003; Benner and Evans 2001). So, in light of sketchy descriptions of unresolved clouds that are available to GCM radiation codes, the ICA seems to be a suitable and tractable standard for 1D radiation codes despite its neglect of 3D transfer. The 1D models that address unresolved horizontal fluctuations that have been discussed thus far, and other operational methods that involve vertical linking of layers, lead to: i) additional computation relative to the straight-up, multi-layer two-stream model; ii) limited, and unrealistic, descriptions of unresolved cloud fluctuations (fluctuations for other components are rarely, if ever, addressed); and iii) most important, biases relative to the full ICA. In an attempt to circumvent these limitations, Barker et al. (2002) and Pincus et al. (2003) introduced the Monte Carlo Independent Column Approximation (McICA) which segregates descriptions of surface–atmosphere structure from the GCM's radiative transfer algorithms.

The essence of McICA is stochastic sampling of subcolumns that are unresolved by a GCM as one sweeps across the necessary spectral integral. To begin, full ICA, domain-average monochromatic radiative fluxes are computed as

$$\overline{F} = \frac{1}{\mathcal{N}} \sum_{n=1}^{\mathcal{N}} F_n \, , \tag{1.62}$$

where F_n is monochromatic radiative flux for the nth subcolumn of the domain. With the correlated k-distribution (CKD) method (e.g., Fu and Liou 1992), broadband radiative fluxes for the nth subcolumn are computed as

$$\mathcal{F}_n = \sum_{k=1}^{\mathcal{K}} F_{n,k} \, , \tag{1.63}$$

where $F_{n,k}$ is the contribution from the kth quadrature point in k-space. Combining (1.62) with (1.63) yields domain-average, broadband fluxes for the full ICA as

$$\overline{\mathcal{F}} = \frac{1}{\mathcal{N}} \sum_{n=1}^{\mathcal{N}} \sum_{k=1}^{\mathcal{K}} F_{n,k} . \tag{1.64}$$

GCM radiation codes typically have $\mathcal{K} \sim 30$–100 so even for a modest value of $\mathcal{N}$, the double sum in (1.64) is intractable in terms of CPU usage.

The McICA method approximates (1.64) simply as

$$\widehat{\overline{\mathcal{F}}} = \sum_{k=1}^{\mathcal{K}} F_{n_k,k} \, , \tag{1.65}$$

where $F_{n_k,k}$ designates a monochromatic radiative flux for a *randomly selected* subcolumn, denoted as n_k, and the circumflex signifies a single sample. The McICA solution (1.65) equals the ICA solution only when all $\mathcal{N}$ columns are identical or when $\mathcal{N} = 1$. In general, McICA's incomplete pairing of subcolumns and spectral intervals ensures that its solution will contain conditional random, but unbiased, errors.

Before proceeding with operational details of this method, it is instructive to show that in the limit of taking $T \to \infty$ samples of (1.65), the ensemble average $\left\langle \widehat{\overline{\mathcal{F}}} \right\rangle$ is identically equal to the ICA. This is easily seen using the CKD method: if there are N_c cloudy columns to select from, then as $T \to \infty$, the nth cloudy column and kth quadrature point will be paired $f_{n,k}$ times such that the expectation of $\left\langle \widehat{\overline{\mathcal{F}}} \right\rangle$ is

$$E\left(\left\langle \widehat{\overline{\mathcal{F}}} \right\rangle \right) = \lim_{T \to \infty} \frac{1}{T} \left\{ f_{1,1} F_{1,1} + \cdots + f_{N_c,\mathcal{K}} F_{N_c,\mathcal{K}} \right\} . \tag{1.66}$$

Since samples are drawn uniformly, all $f_{n,k} = T/N_c$ which reduces (1.66) to

$$E\left(\left\langle\widehat{\widehat{\mathcal{F}}}\right\rangle\right) = \frac{1}{N_c}\left\{F_{1,1} + \cdots + F_{N_c,\mathcal{K}}\right\} \tag{1.67}$$
$$= \frac{1}{N_c}\sum_{k=1}^{\mathcal{K}}\sum_{n=1}^{N_c} F_{n,k}\,,$$

which is the ICA. Hence, McICA is entirely unbiased with respect to the ICA. Since McICA completely decouples the transfer solver from descriptions of unresolved fluctuations, a GCM using McICA is capable of efficiently performing sensitivity studies for a wide range of subgrid-scale assumptions in an unbiased manner.

Equation (1.62) can be partitioned into clear and cloudy contributions, as with all models discussed thus far, and rewritten as

$$\widehat{\widehat{\mathcal{F}}} = (1 - C_{tot})\,\mathcal{F}^{clr} + C_{tot}\sum_{k=1}^{\mathcal{K}} F^{cld}_{n_k,k}\,, \tag{1.68}$$

where C_{tot} is total cloud fraction for the GCM column, and *clr* and *cld* refer to cloud-free and cloudy subcolumns respectively. Note that when aerosols, gases, and surfaces are assumed to be horizontally homogeneous, $\mathcal{F}^{clr}$ is noise-free. Now all $\mathcal{K}$ samples are devoted to cloudy subcolumns as opposed to, on average, $C_{tot}\mathcal{K}$ samples for (1.65). Hence, sampling noise for (1.68) is smaller than that for (1.65). Although in principle, computation of $\mathcal{F}^{clr}$ makes (1.68) more expensive than (1.65), this is a moot point as most GCMs routinely compute $\mathcal{F}^{clr}$ diagnostically in order to compute cloud radiative effects (forcings).

McICA variance σ^2 can be reduced further by taking more than $\mathcal{K}$ samples. This transforms (1.68) into the more general form presented originally by Barker et al. (2002):

$$\widehat{\widehat{\mathcal{F}}} = (1 - C_{tot})\,\mathcal{F}^{clr} + C_{tot}\sum_{k=1}^{\mathcal{K}}\left[\frac{1}{N_k}\sum_{n=1}^{N_k} F^{cld}_{n,k}\right], \tag{1.69}$$

where the total number of samples is

$$\mathcal{N}' = \mathcal{K} + \sum_{k=1}^{\mathcal{K}}(N_k - 1) = \mathcal{K} + \mathcal{M}\,.$$

As such, radiative fluxes for point k are computed for N_k randomly selected cloudy subcolumns, and results are averaged for regular CKD summation.

Räisänen and Barker (2004) presented a procedure to find the optimal set of N_k when McICA noise arises overwhelmingly from clouds. The optimal set of N_k depends on the quantity whose random errors are to be minimized. In a GCM, different predefined sets of N_k could be used based on the state of the Earth–atmosphere column. The most obvious distinction is between land and ocean surfaces. Land surfaces respond rapidly to changes in net solar radiation during daytime, whereas sea surface temperatures change slowly. Therefore, for the SW, it is probably best to base optimization of N_k on CRE at the surface when over land during Sun-up periods but on CRE for lower atmospheric heating when over ocean. Moreover, separate sets of N_k could be defined based on land surface type (e.g., vegetated or snow and ice surfaces). In the LW, optimization of N_k should probably be based on CRE of atmospheric heating regardless of location and time.

Given the size of GCM grid-spacings and the paucity of information regarding subgrid-scale cloud structure, it is natural to expect domain-averaged radiative heating profiles to be characterized by conditional distributions whose widths are wider than that of the Dirac delta distribution. This *natural noise*, or uncertainty, buys some leeway for random noise to be present in subgrid-scale parametrizations. Beyond this natural noise, it may be that GCMs can *consume* additional unbiased random noise generated by subgrid-scale parametrizations with little, or no, statistically significant impact on performance. The obvious, and simple, argument for this is that noise of this type, at or near the spatial and temporal inner-scales of a GCM, is incapable of spawning organized *structures* that significantly affect the trajectory, and perhaps even one-point statistics, of the overall simulated climate.

Figure 1.9 shows the impact of McICA noise on screen temperature simulated by two GCMs. The simulations were 15 days long and 10-member ensembles were run for each rendition of McICA. The benchmark simulation used (1.69) with $\mathcal{M} = 1000$ which almost squelches random noise entirely. This plot shows that the CCCma GCM is insensitive to McICA noise as the fraction of the globe exhibiting differences, relative to the benchmark simulation, that are statistically significant at the α% confidence level is always close to $1-\alpha$ regardless of McICA noise level. These fractions of statistically significant differences are expected for two samples drawn at random from the same population. For the CAM-3 GCM it is clear that it is impacted by noise as noisy renditions of McICA exhibit statistically significant differences over a large portion of the global. However, this sensitivity can be reduced to effectively nothing by using (1.69) with $\mathcal{M} = \mathcal{K}/2$.

1.3.6 Surface albedo

When discussing problems related to fluctuations that are unresolved by conventional GCMs, clouds receive, by far, the most attention. But fluctuations in surface type deserve mention too. Spectral surface albedos $\alpha_s(\lambda)$ are used as lower boundary conditions for atmospheric radiative transfer models. What is usually buried under the convenient blanket of *surface albedo* is actually the fraction of photons not absorbed by anything below either a water surface, a soil surface, or a vegetation canopy. Several studies have examined the reflectance properties of surfaces in detail (e.g., Hapke 1981; Ross 1981; Preisendorfer and Mobley 1986; Verstraete 1987). The purpose of this section is to briefly comment on just a few of the myriad of problems facing specification of surface albedo in global models.

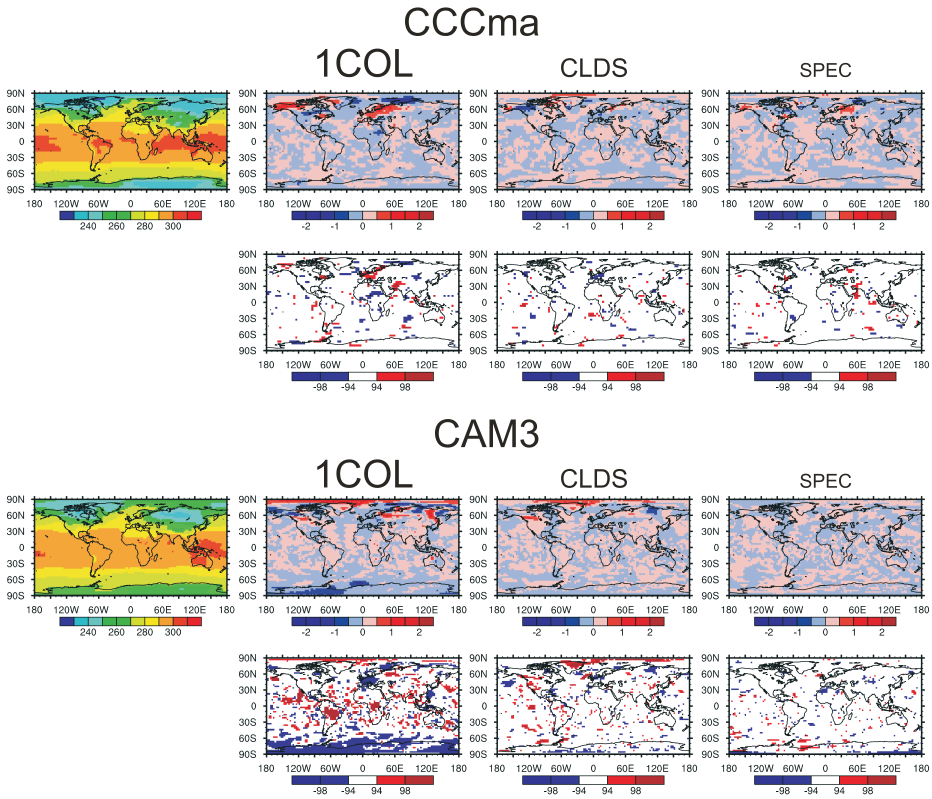

Fig. 1.9. Plots on the left show mean screen temperature (K) for the CCCma GCM and the CAM3 GCM for 15-day simulations using fixed SSTs and sea-ice cover. These results are for benchmark simulations that used almost noiseless versions of McICA. Upper plots in the two sets of plots to the right show screen temperature differences between the benchmarks and three versions of McICA; going from left to right, and as indicated by the font size of the map titles, McICA noise begins large with 1COL [a single sample is drawn to represent all N_k in (1.65)], diminishes to intermediate values for CLDS [which uses (1.68)], and finally to small values for SPEC [using (1.69) with $\mathcal{M} = \mathcal{K}/2$]. See Räisänen and Barker (2004) for details. Lower plots on indicates area where differences were significant at the 95% and 99% confidence levels.

Consider first albedo for land surfaces. Figure 1.10 shows visible and near-IR $\alpha_s(\lambda)$ for various surface types at θ_0 near 60°. Clearly, broadband radiative transfer models face the same problem with surface albedo as they do with atmospheric constituents: they require spectrally-weighted values, but the necessary spectral irradiances needed to compute mean values, for relatively broad bands, are not available. Generally, simple uniform weightings are applied and surfaces are assumed to be perfectly Lambertian. In many applications, only a gross distinction is drawn between albedo in a few bands across the solar spectrum (e.g., $<0.7\,\mu$m and $>0.7\,\mu$m). Likewise, dependencies on θ_0 are generally crude

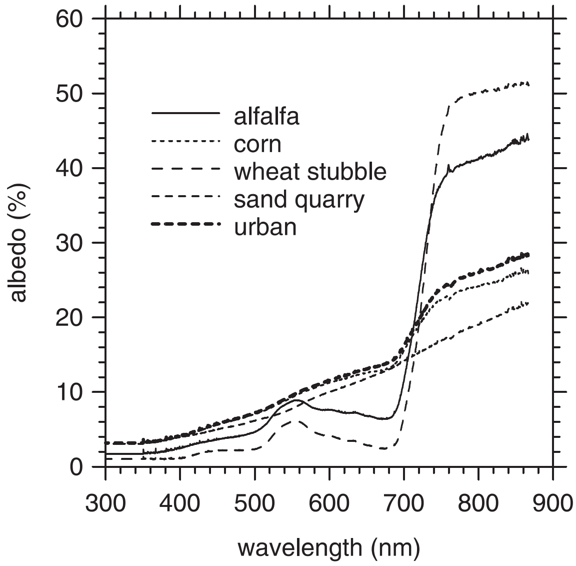

Fig. 1.10. Examples of spectral surface albedos for various surface types as functions of wavelength. These data were collected during spring in OK, USA. (Data courtesy of Z. Li 2000.)

and often do not distinguish between direct and diffuse albedos (but again, this partition actually requires solution of the radiative transfer algorithm).

Owing to the fact that roughly two-thirds of Earth's surface is covered by open water, albedo of water surfaces is an important quantity in a global model. There have been several studies that examined how the albedo of water surfaces with wind-generated waves depends on μ_0 and wind speed $|\mathrm{v}|$ (e.g., Cox and Munk 1956; Payne 1972; Preisendorfer and Mobley 1986). Cox and Munk's method assumes that the slopes of wave facets follow a Gram–Chevalier (i.e., Gaussian-like) distribution that depends on $|\mathrm{v}|$ and that only Fresnel reflection need be considered. Despite it being a single-reflection model that does not account for spatial correlation of wave facets, it has been used successfully to infer $|\mathrm{v}|$ from observations of sun glint (its original intention).

Figure 1.11 shows a curve fit to Payne's observations (Briegleb et al. 1986) along with results from Cox and Munk's model (Hansen et al. 1983). Clearly the Cox and Munk parametrization captures the essence of ocean albedo. It can, however, be augmented slightly to account for the effects of whitecaps (Monahan and O'Muircheartaigh 1987), suspended particulates, and bottoms (in shallow areas). Multiple reflection effects, which depend directly on spatial structure of wave forms, are likely to be important for radiances, inside certain ranges of illumination and viewing, but are second-order as far as fluxes are concerned.

Obviously, if one believes there is an important feedback to capture between ocean absorption of solar radiation and near-surface winds, it is essential that a wind-speed dependent description of ocean albedo be employed in global models.

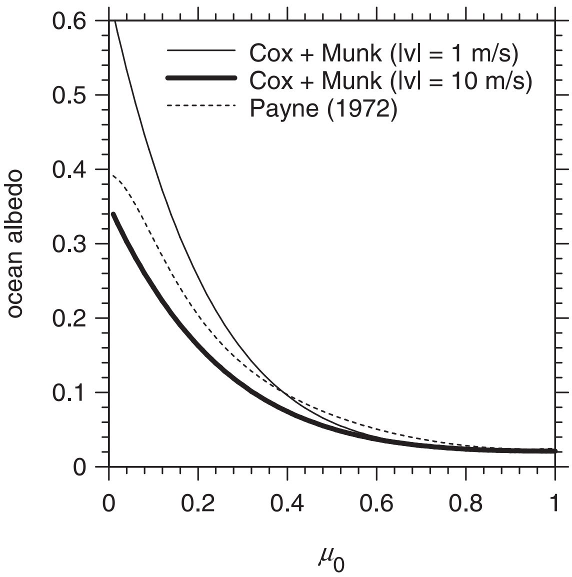

Fig. 1.11. Dashed line shows a curve fit to observed ocean albedo (Payne 1972). Other lines are predictions by the Cox and Munk wave slope approach for two wind speeds $|\mathbf{v}|$ assuming Fresnel reflection.

Likewise, at a similar level of concern, there should be an explicit dependence on the quality of illumination; that is, a distinction between direct- and diffuse-beam surface irradiance.

Computation of albedo for a totally snow-covered surface is a fairly straightforward problem because snow is optically dense. As a result, plane-parallel, homogeneous conditions can be satisfied fairly easily which makes for reliable application of two-stream approximations provided one has a reasonable idea of crystal size and amounts of impurities (see Warren 1982). Complications and biases arise, however, when dealing with snow amidst vegetation. For example, masking of snow by vegetation, and vice versa, exhibits a strong dependence on illumination angle (e.g., Otterman 1984). Another example is snow in mountain regions. Assume that almost all the snow exists in shaded areas. If the sky is overcast with only diffuse surface irradiance, mean albedo would be close to a linear weighting based on fractional area of snow and exposed rock. If the majority of surface irradiance is direct-beam, mean surface albedo would be close to that of the rock if the majority of snow is on the shaded side. This points to a more general issue: the proper mean albedo to be used in a 1D radiative transfer model is not the areal-weighted mean, but rather the irradiance- and areal-weighted mean. To do this properly, however, requires a solution for surface irradiance beforehand, which does not exist, as well as consideration of surface tilt geometry.

It is expected that albedo of sea-ice will require increasing attention as representation of sea-ice in GCMs continues to improve (Kreyscher et al. 2000; Bitz

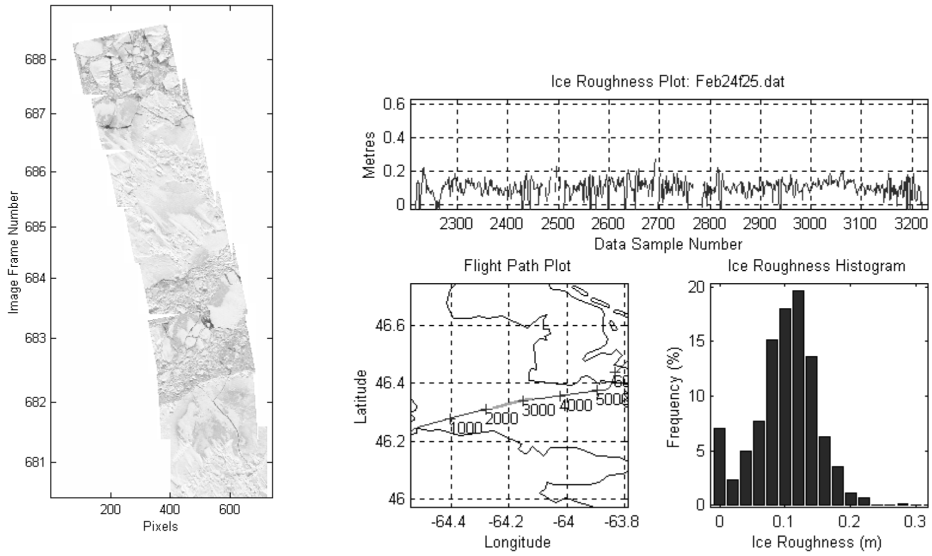

Fig. 1.12. Plot on the left shows imagery of sea-ice in Northhumberland Strait, Canada (image is about 0.5 km wide). Upper plot on the right shows normalized ice altitudes as detected by a helicopter-mounted laser altimeter tracking down the centre of the image on the left. Lower plots on the right show a map of the transect and frequency distribution of ice altitude. (Data courtesy of I. Peterson, 2001.)

et al. 2002). It may be that different types of ice can be diagnosed and a μ_0 dependence of albedo assigned to each type. Figure 1.12 shows an example of the complexity of sea-ice. Presumably the roughness characteristics of these surfaces impacts albedo? The same goes for wind-generated sastrugi that exist over vast tracts of Antarctica (see Warren et al. 1998). However, we are undoubtedly a long way off performing actual on-line radiative transfer calculations for surfaces as complex as these.

Regarding representing radiative transfer for vegetated surfaces inside GCMs, much work has been done by Pinty et al. (2006). The essence of their work is to utilize the standard two-stream solutions with optical properties suitably modified to represent the discrete scattering elements found in vegetation canopies and to alter these quantities in such a way that the two-stream mimics corresponding results obtained by 3D Monte Carlo simulations. The attraction of this approach is that the surface system becomes an extra layer at the base of the regular atmospheric column. So instead of an atmospheric radiative transfer code using N layers, it uses $N + 1$ layers with an underlying description of ground (not collective surface) albedo. Moreover, if there is a distribution of surface-vegetation types inside a GCM column, they can be included in a stochastic subgrid-scale generator (cf. Räisänen et al. 2004) and used in conjunction with the McICA approach.

1.4 1D vs. 3D radiative transfer for cloudy atmospheres: should global modellers be concerned?

Thus far only results from 1D radiative transfer codes have been shown and discussed. The assumption all along has been that the ICA is a justifiable standard for GCM-style radiation solvers to aim for. This goal has been obtained by the Monte Carlo class of ICA codes. The lingering question, however, is: are systematic flux and heating rate differences between the ICA and full 3D important for numerical simulation of climate? We are just entering an era with supercomputing that enables us to address this question, and progress has already been made. Two points of concern are reiterated here: i) are domain-average fluxes provided by the ICA sufficient; and ii) how important are interactions between cloud and radiation at scales that are unresolved by conventional GCMs? The former addresses 3D radiative transfer squarely, while the latter, which is essentially a 3D issue, can be addressed to some extent by the ICA.

1.4.1 Domain-average fluxes

When contrasting 1D and 3D radiative transfer it is helpful to study details at scales finer than large domain-averages to help appreciate differences. As an example, consider the 2D cloud shown in Fig. 1.13. This stratiform cloud is moderately inhomogeneous for its range of liquid water path (LWP) is fairly large yet its physical aspect ratio is not. Vertically-projected cloud fraction over this 10 km domain is 0.9, mean visible optical depth is 18.9, and corresponding ν_{mom} is 2.6. Even water vapour content, as expected, varies in the horizontal. Figure 1.14 shows heating rates for 3D transfer and the ICA at several different solar zenith angles. In a plot like this differences between 3D and ICA transfer are obvious. Most notably, ICA casts cloud shadows vertically regardless of sun angle. A more subtle difference is in cloud heating; clouds absorb more for 3D transfer at small μ_0 and less at large μ_0.

Figure 1.15 shows corresponding domain-average values. Domain-average atmospheric absorptances for 3D and ICA are virtually identical despite the clear spatial differences seen in Fig. 1.14. Albedo is overestimated very slightly by the ICA for most μ_0 (but much less so than outright neglect of variability), and underestimated only at very small μ_0 on account of side illumination for 3D transfer (testified to in Fig. 1.14 by elimination of direct-beam transmittance at small μ_0). The centre plot of Fig. 1.15 shows that mean photon pathlengths differ little between ICA and 3D, except again at small μ_0 where ICA pathlengths are slightly longer. The rightmost plot shows that the mean numbers of times reflected photons are scattering by droplets are essentially identical for ICA and 3D. For transmittance, however, photons in the 3D simulation experience fewer scattering events for all μ_0, especially small μ_0 where photons frequently exit cloud sides in downward directions after few scatterings. Despite these differences, it is still interesting to note again that domain-average atmospheric absorptances are almost identical (see Barker et al. 1998).

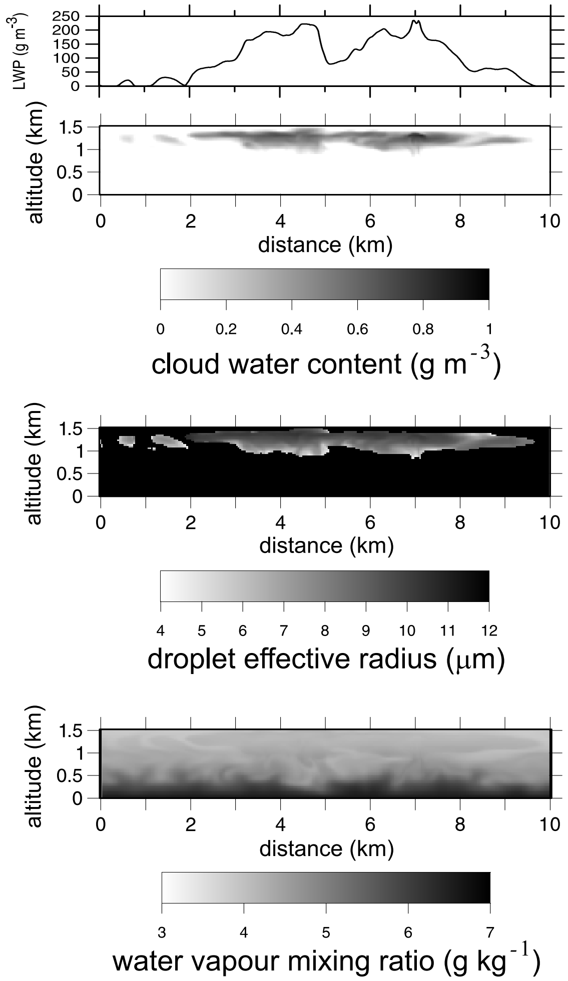

Fig. 1.13. Top plot shows visible optical depth of cloud for a 10 km section of cloud simulated by a cloud system-resolving model with 25 m horizontal and vertical grid-spacings. Beneath it is liquid water content, droplet effective radius, and water vapour mixing ratio. (Data courtesy of J.-P. Blanchet, 2001).

This example serves to demonstrate what several studies have found: there are obvious local differences between 3D and ICA, but as soon as the domain size exceeds a few characteristic cloud cell dimensions, differences between 3D and ICA domain-average radiative quantities diminish rapidly.

In the past, small numbers of cloud configurations were used to address differences between 3D radiative transfer and approximate solutions (e.g., McKee and Cox 1974; Welch and Wielicki 1985; O'Hirok and Gautier 1998; Barker et al. 1999). Barker et al. (2003) intercompared domain-average, broadband irradiances for cloudy atmospheres as computed by several 1D and 3D solar transfer

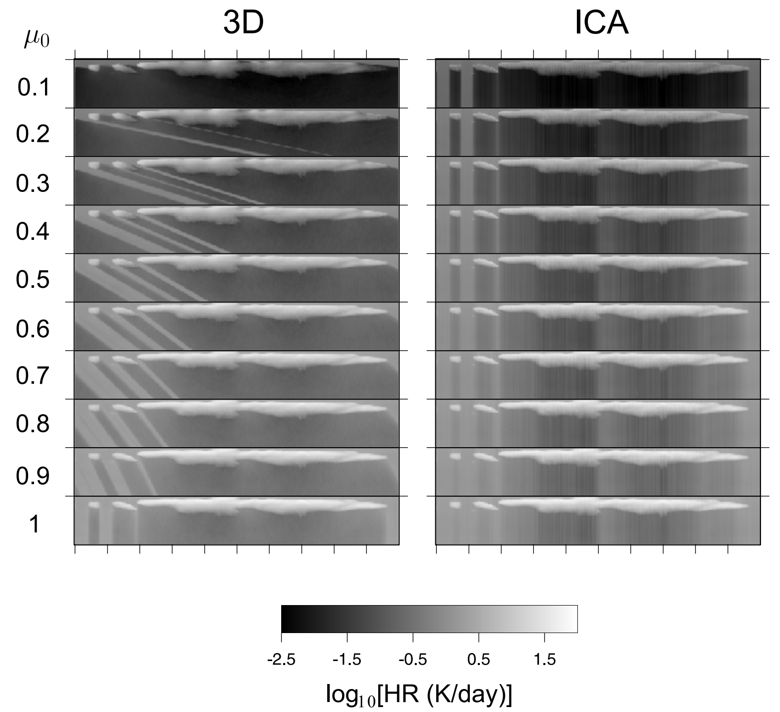

Fig. 1.14. Heating rates for the cloud field shown in Fig. 1.13 for various solar zenith angles θ_0 ($\mu_0 = \cos\theta_0$ are listed on the left). Left column is for 3D radiative transfer while right column is for the ICA model. All calculations were performed with a Monte Carlo photon transport algorithm; the 3D simulations used 25 m horizontal grid-spacings while the ICA used an extremely large setting.

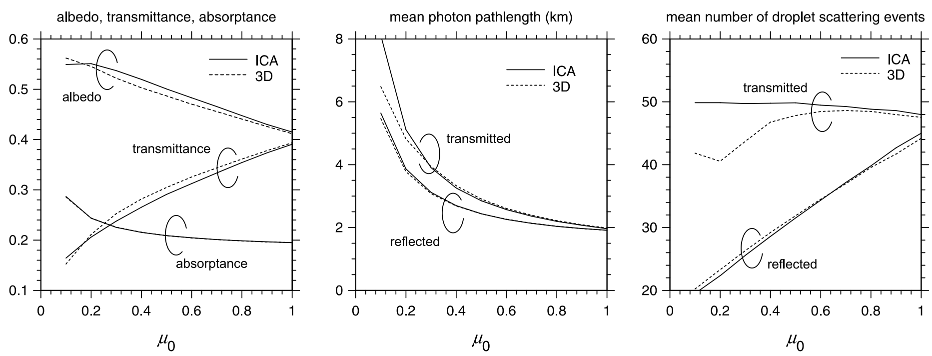

Fig. 1.15. Left plot shows domain-average albedo, transmittance, and atmospheric absorptance as functions of cosine of solar zenith angle μ_0 for 3D and ICA simulations performed on the field shown in Fig. 1.13 Middle and right plots show corresponding mean photon pathlengths (below cloudtop) and mean number of droplet scattering events for photons that are reflected to space and transmitted to the surface.

codes, but again used only a half-dozen or so cases. Cole et al. (2005a), however, used thousands of cloud fields that were produced by a GCM whose conventional cloud parametrization was replaced by a 2D cloud system-resolving model (CSRM). Such super-parametrized GCMs, known officially as Multi-scale Modeling Framework (MMF) GCMs, are developing rapidly (see Randall et al. 2003). For Cole et al.'s (2005a) study, CSRM domains had 64 columns with 4 km horizontal grid-spacing Δx, 24 vertical layers and a timestep of 20 s, and were aligned east to west (Khairoutdinov and Randall 2003). Each CSRM was forced by large-scale tendencies updated every GCM timestep, and provided horizontally-averaged tendencies back to the GCM. The CSRM prognostic thermodynamic variables included liquid/ice water moist static energy, total non-precipitating water, and total precipitating water. All simulations started on September 1, 2000. Global arrays of CSRM data were sampled and saved every 9 model hours. Allowing the model a short spin-up period, radiation calculations were performed on model output for December 2000. This amounted to solar calculations being performed on over 300,000 fields.

Figure 1.16 shows monthly-mean differences between 2D radiative transfer and the ICA for upwelling SW at the TOA. The largest TOA differences are associated with tropical deep convective clouds with secondary maxima across the southern ocean storm belt partly because of excessive cloudiness and large solar inputs. The adjacent plot shows the distribution of flux differences as a function of latitude and μ_0. Suppression of photon leakage out the sides of convective clouds in the ITCZ by the ICA at large μ_0 explains why it overestimates reflected flux. Conversely, the ICA does not account for illumination onto cloud

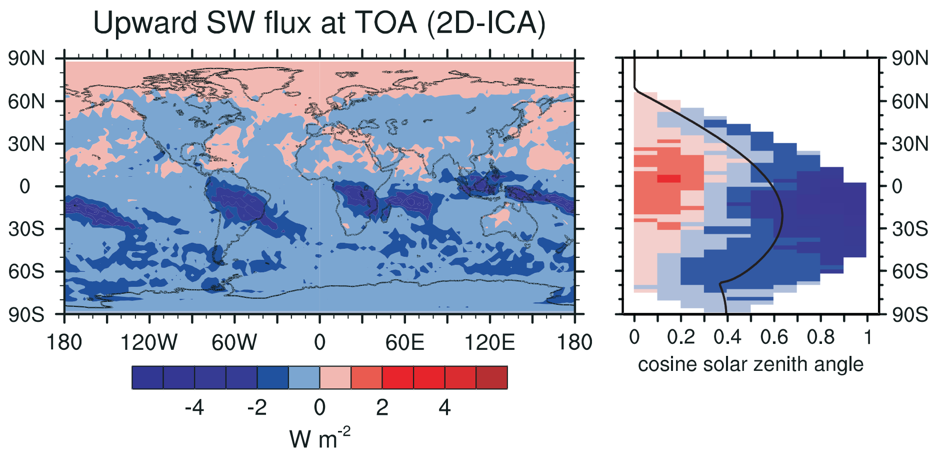

Fig. 1.16. Differences for monthly-mean upwelling SW flux at TOA when radiation calculations are done with the ICA and 2D radiative transfer. Global mean value is 104.7 W m^{-2} for the 2D case. Plot on the right shows corresponding mean values as a function of μ_0 and latitude. Solid line indicates monthly-mean μ_0.

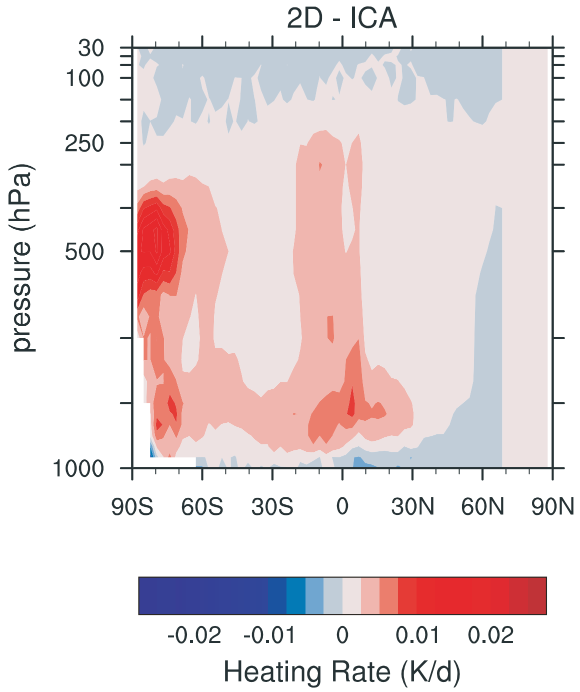

Fig. 1.17. Monthly-mean, zonal cross-section of differences in SW heating rate between 2D radiative transfer and the ICA as a function of latitude and altitude.

sides, so at small μ_0 it underestimates reflected flux (e.g., Welch and Wielicki 1985; O'Hirok and Gautier 1998).

Figure 1.17 shows a vertical cross-section of monthly-mean SW heating rate differences between 2D and ICA. This shows clearly the impact of cloud side illumination at cloud-bearing altitudes. Namely, when significant side illumination occurs, as with 2D transfer, clouds absorb more radiation relative to the ICA approach.

Using data from O'Hirok and Gautier (2005), Cole et al. (2005a) also addressed the question of drawing too many conclusions from their results given $\Delta x = 4$ km. They concluded that if Δx was reduced to about 0.5 km, values shown in Fig. 1.16 could roughly double in certain areas due to cloud fluctuations becoming increasingly resolved. At that point, differences between 3D radiative transfer and the ICA would begin, at times, to rival those that occur between ICA and conventional GCM treatments (see Cole et al. 2005a; Stephens et al. 2004).

The point to remember with conventional GCMs is that only gross descriptions of cloud structure are available. Often this amounts to just mass of condensed water in a layer and a corresponding estimate of cloud fraction. We are just beginning to parametrize other details like droplet concentration and size, variance of water content, and vertical overlap rates. While one-point distributions of clouds can be generated stochastically and used with the McICA method (e.g., Räisänen et al. 2004), it is still an open question as to whether it is worth going the extra step and assuming (i.e., imposing) horizontal structure which is required to perform 3D radiative transfer. It may be that the differences discussed in this section are significant and that these extra assumptions are well worth it, but it will require a suitable and efficient algorithm for generating subgrid-scale clouds and an equally efficient 3D radiative transfer model. Nevertheless, all that would be required would be domain-averaged and spectrally-integrated flux profiles. We know already that random noise is a minor issue for weather forecasting and climate modelling (cf. section 1.3.5.5 on McICA), so reasonable numbers of photons in a 3D Monte Carlo simulation (especially for SW transfer; see Evans and Marshak 2005) would likely suffice.

1.4.2 Unresolved cloud–radiation interactions

Even if a GCM computes domain-average fluxes based on 3D radiative transfer, the remaining question is: do conventional GCMs, with horizontal grid-spacings on the order of 100 km or more, resolve cloud-radiation interactions sufficiently well? This crucial question was one of the prime factors behind the push toward MMF-GCMs (Grabowski 2001; Randall et al. 2003). By definition this question cannot be answered with a conventional GCM. One must be content to use either stand-alone CSRMs or an MMF-GCM. Obviously the latter is more preferable, but more expensive, as large-scale circulation comes into play explicitly.

Presumably, this question can be addressed to a great extent using the ICA (e.g., Fu et al. 1995); that is, allow the CSRMs to experience local radiative heating rates regardless of whether they are computed using 3D transfer or not. This is what Cole et al. (2005b) did using an MMF GCM with a CSRM whose horizontal grid-spacing was 4 km. In a series of experiments, they demonstrated that allowing the CSRMs to respond to cloud–radiation interactions at the 4 km scale was roughly as important as getting domain-average fluxes correct. Incorrect domain-average fluxes were provided by a standard two-stream model with maximum-random overlap of homogeneous clouds. Hence, domain-average errors were close to what could be expected if a common GCM radiative transfer algorithm were to be replaced by the McICA algorithm.

Figure 1.18 shows the impact on cloud radiative effects at the TOA due to inclusion of unresolved interactions between clouds and radiation (pers. comm., J. Cole 2005). Experiment 1 served as the benchmark for it utilized heating rates at 4 km and also provided the GCM with proper (ICA) domain-average fluxes. Experiment 4 utilized heating rates at 4 km too but incorrect domain-averages were passed back to the GCM. Evidently this was not important for this seasonal simulation. For Experiments 2 and 3, on the other hand, heating rates were averaged horizontally across the domains and used by the CSRMs. Experiment 2 passed correct domain-average fluxes back to the GCM while Experiment 3 did not. Clearly, omission of heating rates at the CSRMs' inner-scale are most important for this experiment. The significance of this result rests in the realization that getting proper domain-averages in a GCM is one

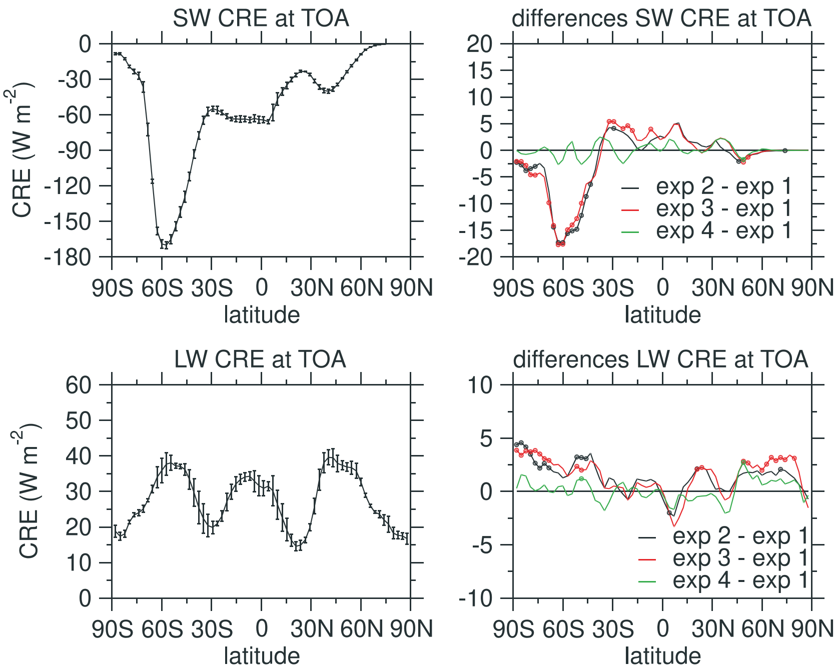

Fig. 1.18. In the left column are plots of zonal-mean, time-averaged SW and LW cloud radiative effects (CRE), also known as cloud radiative forcing, for December as computed by an MMF GCM. Error bars indicate one standard deviation as realized by a five-member ensemble of the benchmark simulation (exp 1). Plots on the right show differences between various simulations and exp 1. See text for details. Dots indicate when a difference is significant at the 95% confidence level. (Data courtesy of J. Cole, 2005.)

thing, but how can one expect to account for unresolved interactions between clouds and radiation in a conventional GCM cloud parametrization where clouds are not resolved anywhere near fundamental cloud formation-dissipation scales? The answer is far from obvious, and we might run out of time trying solve it, for eventually either MMF-GCMs will become commonplace or GCMs will simply become, in essence, global CSRMs. In either case, the issue of subgrid-scale parametrization will diminish over time. Then again, conventional GCMs will likely continue to serve purposes, and if they continue to be used in important roles, as they are today, progress will be required on cloud-radiation interactions of the kind discussed here.

1.5 Remote sensing of cloudy atmospheres and global climate modelling

For some time now the most valuable data for assessing GCMs have come from the Earth radiation budget satellite missions, namely Earth Radiation Budget Experiment (ERBE) and Clouds and the Earth's Radiant Energy System (CERES). For the most part, these datasets are used to determine monthly-mean radiation budgets and cloud radiative effects for diagnostic comparison against corresponding values predicted by GCMs. Yet even here there are still issues and uncertainties such as radiance-to-flux conversion and sparse sampling (e.g., Loeb et al. 2003). Recently these Earth radiation budget datasets have been merged with other datasets and radiative quantities have been sorted according to dynamical regime in an attempt to identify the conditions responsible for the wide disagreement observed among GCMs with respect to estimates of cloud feedback (cf. Bony et al. 2004). Additionally, attempts have been made to bring models and observations closer together via dataset emulators such as the so-called ISCCP simulator (Webb et al. 2001) where GCM fields, like cloud fraction and optical depth, are converted, without actually performing radiative transfer calculations, to resemble products inferred from satellite data. The alternative to this approach is to apply more sophisticated radiative transfer algorithms to GCM data, thereby producing radiance estimates that can be compared directly to satellite measurements.

For the past 15 years or so, surface-based cloud-profiling radars (CPRs) have provided much information about the vertical and horizontal structural characteristics of clouds (e.g., Clothiaux et al. 1999). Recently, NASA's CPR-bearing CloudSat satellite was launched into a Sun-synchronous orbit (see Stephens et al. 2002). CloudSat is flying in close formation with several other satellites in the so-called *A-train* constellation. When data from these satellites are merged, they have the strong potential to yield invaluable insights into the structure of clouds at the global scale. There are, however, many issues that have to be grappled with first.

The CPR emits pulses of electromagnetic radiation that are scattered by particles in proportion to the sixth power of particle radius. Hence, CPRs are quite sensitive to large cloud droplets, but have difficulty sensing small droplets. It is immediately clear then that CPR data have to be augmented with data from measurements that are sensitive to other moments of particle size distributions. Hence the need to collocate CPR data with other data.

In addition, satellite-based CPRs suffer from the same sampling issues as do aircraft and instruments fixed at the surface. Astin et al. (2001) have shown that in broken cloud conditions, transects may have to be several hundred kilometres long before significant reductions can be realized in the confidence intervals for estimates of cloud fraction of the domain from which the transect was drawn. Figure 1.19 illustrates the situation one will encounter with both CPRs fixed on the surface (as this one is), or on aircraft or satellite. It shows the 512-km domain of a CSRM which is taken here to be a grid-cell of a GCM. What the GCM (or the CSRM) requires is a time series of the domain. What the CPR

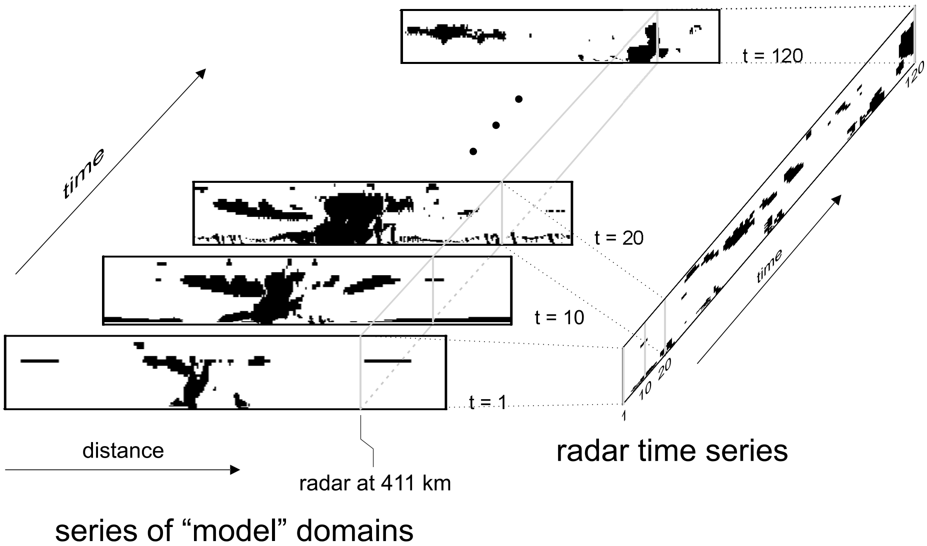

Fig. 1.19. On the right is a sampled time series of cloud masks for a 512-km domain produced by a CSRM (Fu et al. 1995). Imagine that a surface-based CPR is fixed at 411 km along the domain. Stringing together the 120 snapshots at 411 km leads to the CPR-domain shown on the right. A GCM or NWP model would want what is on the left, but the radar produced what is on the right. Clearly, in this particular case, what the radar samples is a rather poor representation of the sequence of domains. Satellite-based CPRs will be subject to this sampling issue as well.

(fixed here at 411 km across the domain) gives is a time series of cloud that drifts over it. As Fig. 1.19 shows, the time series of cloud obtained at 411 km appears to contain only a slim semblance of the domains.

Despite these complications with CPR data, NASA's CloudSat satellite, with its 94 GHz CPR in conjunction with the lidar on CALIPSO, and the passive sensors on AQUA, should provide an interesting global view of the coincidental vertical and horizontal structure of clouds. Figure 1.20 shows an example of CloudSat data along with near-simultaneous 1-km GOES visible and thermal imagery and NEXRAD surface precipitation radar data. Clearly CloudSat has pinpointed precipitating clouds and appears to have even sensed the shallow clouds immediately east of the Florida–Georgia border.

Data from CloudSat and the A-train will enable global-scale calculations of information such as, for example, radiative sensitivities for climate model parameters like cloud overlap decorrelation lengths which are required by the more sophisticated GCM parametrizations. This is because cloud fractions in distinct layers will be reported. To illustrate, if c_k and c_l are fractional amounts of cloud in layers k and l as reported by CloudSat, and if A_c is total cloud fraction, define

$$A_c = \alpha_{k,l} c_{k,l}^{\max} + (1 - \alpha_{k,l}) c_{k,l}^{\mathrm{ran}} \,, \tag{1.70}$$

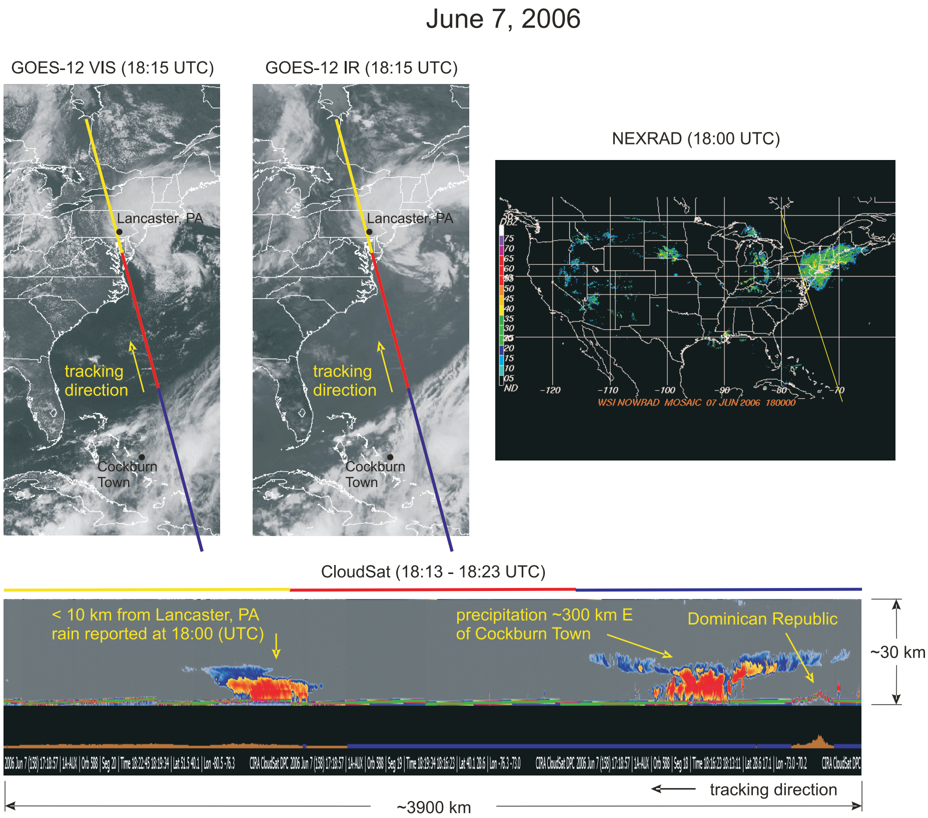

Fig. 1.20. Lower plot shows an almost 4000 km long transect of CPR reflectivities measured by CloudSat. These uncalibrated data were produced only a week after CloudSat's radar was switched on. Nevertheless, it shows an unprecedented view of clouds that up until then would have been restricted to the passive GOES images shown in the upper left and the NEXRAD surface precipitation radar composite shown in the upper right. CloudSat's colour-coded cross-section is shown on the GOES imagery and the total trajectory is shown on the NEXRAD image.

where

$$\begin{aligned} c_{k,l}^{\max} &= \max\left(c_k, c_l\right) \,, \\ c_{k,l}^{\mathrm{ran}} &= c_k + c_l - c_k c_l \,. \end{aligned} \tag{1.71}$$

The overlap parameter $\alpha_{k,l}$ in (1.70) is defined as

$$\alpha_{k,l} = \exp\left[-\int_{z_k}^{z_l} \frac{\mathrm{d}z}{\mathcal{L}_{cf}(z)}\right] \,, \tag{1.72}$$

where $\mathcal{L}_{cf}$ is decorrelation length for overlapping fractional cloud, and z is altitude (Hogan and Illingworth 2000; Bergman and Rasch 2002).

Changes to $\mathcal{L}_{cf}$ impact SW fluxes primarily through changes to A_c and $p(\tau)$. As shown in section 1.3.5.3, the first two moments of $p(\tau)$ are often sufficient to capture domain-average SW fluxes. Therefore, following Barker and Räisänen (2005), the radiative sensitivity for $\mathcal{L}_{cf}$ can be expressed as

$$\frac{\partial F}{\partial \mathcal{L}_{cf}} \approx \frac{\partial F}{\partial A_c}\frac{\partial A_c}{\partial \mathcal{L}_{cf}} + \frac{\partial F}{\partial \overline{\tau}}\frac{\partial \overline{\tau}}{\partial \mathcal{L}_{cf}} + \frac{\partial F}{\partial \sigma_\tau}\frac{\partial \sigma_\tau}{\partial \mathcal{L}_{cf}}\,, \tag{1.73}$$

where $\overline{\tau}$ is mean cloud optical depth for the cloudy part of the domain, and σ_τ is corresponding relative standard deviation of τ. Each derivative in (1.73) depends on cloud structure inside the domain as well as other parameters such as water vapour and temperature profiles, surface conditions, and θ_0. Note also that the leading term in the three terms on the RHS of (1.73) are themselves sensitivities that can be computed separately holding all else constant, including $\mathcal{L}_{cf}$ (cf. Schneider 1972).

With the stochastic subcolumn generator developed by Räisänen et al. (2004) it is straightforward to compute how cloud properties and F depend on $\mathcal{L}_{cf}$ from which corresponding derivatives can be estimated numerically. Figure 1.21 shows global estimates of $\partial F/\partial \mathcal{L}_{cf}$ using data for a single day (January 1) generated by an MMF GCM (Khairoutdinov and Randall 2001). The global-mean value for net radiation (SW + LW) is $1.76\,\mathrm{W\,m^{-2}\,km^{-1}}$ with $1.99\,\mathrm{W\,m^{-2}\,km^{-1}}$ in the SW and just $-0.23\,\mathrm{W\,m^{-2}\,km^{-1}}$ in the LW. Perhaps as expected, the largest sensitivities are in the tropics where minor deviations to the overlap rate of

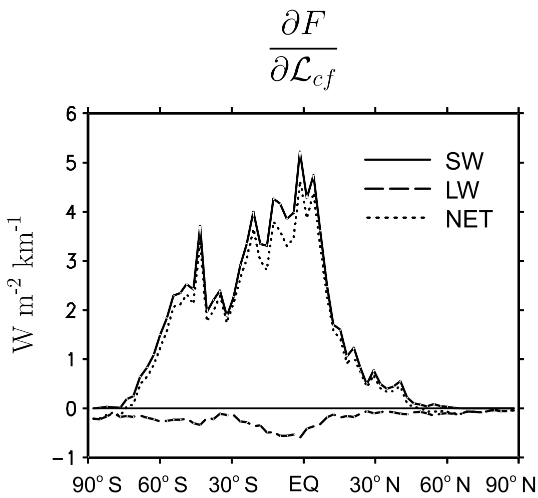

Fig. 1.21. Radiative sensitivities $\partial F/\partial \mathcal{L}_{cf}$ for cloud fraction vertical decorrelation length $\mathcal{L}_{cf}$ computed with all else held constant. SW, LW, and NET (SW + LW) components are shown as functions of latitude. These estimates were computed using data from an MMF GCM simulation. It is anticipated that plots like this will be available from data collected by CloudSat and the other A-train satellites.

towering clouds coupled with high solar irradiance conspire to affect large TOA albedo changes. The hope is that a corresponding analysis can be conducted using inferences from A-train data.

1.6 Concluding remarks

This central thesis of this volume is scattering of radiation (light). Given limitations on length, this chapter focused on treatment of solar radiative transfer in global climate models (GCMs). The intention was to give readers, especially upper-level undergraduates and entry-level graduates, a *taste* of some of the light scattering-related issues facing computation of radiative fluxes in global models. Emphasis was on some of the macroscopic issues regarding solar radiative transfer for cloudy atmospheres.

After discussing the central role played by radiation in global climatology and analyses of climate, both real and simulated, the mainstay of GCM radiative transfer solvers was discussed; two-stream approximations. Limitations of two-streams were mentioned and some techniques were reviewed for extending the application of basic two-streams to address fluctuations in cloud density that are unresolved by conventional GCMs. The obvious limitation is the fact that clouds are never homogeneous in the horizontal or the vertical, and so the basic assumptions upon which two-streams are built are violated repeatedly in GCMs. Regarding the macroscopic aspects of clouds, this translates into descriptions of horizontal fluctuations of cloud properties across a GCM layer as well as how these fluctuations stack up in the vertical. This discussion finished with the Monte Carlo Independent Column Approximation (McICA) which decouples description of unresolved fluctuations in the medium from the radiative transfer solver and so eliminates biases that analytic two-stream extensions are bound to possess. Hence, McICA is able, to the same extent as the full ICA, to address all descriptions of horizontal fluctuations and vertical overlap patterns. The problem is that conventional GCM cloud parametrizations are still in their infancy when it comes to describing the nature of unresolved cloud structure, and so at the moment, McICA within a GCM can be provided only with limited information. The hope is that a synthesis of data from a host of sensors will help guide production and assessment of these much needed aspects of cloud parametrization. Data from the active sensors in the A-train of satellites (see Stephens et al. 2002) as well as from the Atmospheric Radiation Measurement (ARM) program (Stokes and Schwartz 1994) and the BALTEX Bridge Cloud (BBC) campaign, should help immensely, but it is still too early to tell as extensive numerical end-to-end simulations of what we know these instruments are sensing have yet to take place. Having said this, the unbiased nature of McICA is, however, only as good as one's willingness to neglect 3D radiative transfer effects on fluxes.

On this last point there are two levels of concern. First, are domain-average fluxes provided by the ICA sufficient for climate simulation? Global estimates of differences between the ICA and 3D radiative transfer were provided in section 1.4.1 (see Cole et al. 2005a). In the framework of conventional GCMs, with only limited amounts of information regarding unresolved cloud structure, the answer is probably: yes, the ICA is sufficient. This is because to go beyond the ICA requires explicit cloud fields as opposed to descriptions of one-point probability distributions for horizontal variations and statistical descriptions for vertical overlap. GCMs are barely in a position to provide these descriptions let alone make the leap to conjuring up full 3D, even 2D, unresolved cloud fields. Again, data like those from the satellite A-train should help address this concern. Nevertheless, it might be worthwhile performing some GCM sensitivity experiments that employ a simple stochastic cloud field generator [like that developed by Räisänen et al. (2004) but including horizontal structure] to see if the fairly subtle, yet systematic, effects of 3D transfer impact global climate simulations.

The second question regarding 3D effects is: are interactions between cloud and radiation at scales that are unresolved by conventional GCMs important for climate simulation? As mentioned in section 1.4.2, this effect can be addressed partially using the ICA method. This is how Cole et al. (2005b) investigated this issue using an MMF GCM in which the cloud parametrization consisted of a 2D cloud system-resolving model (CSRM). In essence, the CSRM provides explicit cloud fields (i.e., no need to invoke parametrizations to describe unresolved fluctuations) so the ICA can be applied directly to the CSRM fields and the CSRMs can either evolve based on local radiative heating rates or domain-averaged heating rates. Likewise, either ICA domain-average fluxes or incorrect values based on a conventional GCM radiation solver (e.g., one that makes simple assumptions about clouds at scales unresolved by the host GCM) can be passed back to the host GCM. There is nothing, except computational limitations perhaps, stopping one from repeating Cole et al.'s experiments using 3D radiative transfer models. The disconcerting conclusion they came to was that, for their experiments in particular, cloud-radiation interactions at scales unresolved by the host GCM appear to be approximately as important as getting the domain-average flux profiles correct (i.e., via the ICA or McICA). This is disconcerting because it is very difficult to see how these interactions can be parametrized in a conventional GCM to an extent that would be considered to be even remotely satisfying.

There are many aspects to GCM radiative transfer calculations that were not addressed explicitly in this chapter. Some of them have been discussed elsewhere in this volume. For example, scattering by ice crystals is dictated by the size, geometric structure, and orientation of crystals, but as yet there is little consensus on any of these properties. As such, representation of scattering by ice crystals in GCM radiation codes is still at the stage of fiddling with gross properties, like asymmetry parameter, in order to satisfy model simulation of global radiation budgets. On the other hand, treatment of absorption of radiation by atmospheric constituents has been addressed only in passing throughout this volume. Likewise, relatively little has been said about measurement of Earth's radiation budget by satellites as a means of assessing GCM simulations, though an entire chapter could easily be devoted to this subject.

A Appendix: Two-stream approximations

The purpose of this appendix is to clarify two-stream approximations. Begin by restating the azimuthally-averaged 1D equation of transfer [see (1.19)] as

$$\begin{aligned} \mu \frac{\mathrm{d}I(\tau,\mu)}{\mathrm{d}\tau} &= -I(\tau,\mu) + \frac{\omega_0}{2}\int_{-1}^{1} p(\mu;\mu')I(\tau,\mu')\,\mathrm{d}\mu' \\ &\quad + \frac{F_0}{4}\omega_0 p(\mu;\mu_0)\,\mathrm{e}^{-\tau/\mu_0}\,, \end{aligned} \tag{A1.1}$$

where I is radiance, F_0 is incoming solar at the TOA, μ is cosine of zenith angle, μ_0 is cosine of solar zenith angle, τ is optical thickness, and ω_0 is single scattering albedo. Define

$$F^{\pm}(\tau) = \int_0^1 \mu I(\tau,\pm\mu)\,\mathrm{d}\mu \tag{A1.2}$$

as upwelling and downwelling irradiances. Going a step further, let $I(\tau,\pm\mu)$ be defined as

$$I(\tau,\pm\mu) = \sum_{m=0}^{\infty} i_m(\tau)\,P_m(\mu) \tag{A1.3}$$

where $P_m(\mu)$ is the mth-order Legendre polynomial. Hence, (A1.2) becomes

$$F^{\pm}(\tau) = \int_0^1 \mu \sum_{m=0}^{\infty} i_m(\tau)\,P_m(\mu)\,\mathrm{d}\mu. \tag{A1.4}$$

By applying the hemispheric operators $\int_0^1 \mathrm{d}\mu$ and $\int_{-1}^0 \mathrm{d}\mu$ to (A1.1), using (A1.4), and dropping explicit notation of dependence on τ yields the coupled equations:

$$\left\{ \begin{aligned} \frac{\mathrm{d}F^+}{\mathrm{d}\tau} &= \int_0^1 \sum_{m=0}^{\infty} i_m P_m(\mu)\,\mathrm{d}\mu - \frac{\omega_0}{2}\int_0^1\int_{-1}^1 p(\mu;\mu')\sum_{m=0}^{\infty} i_m P_m(\mu)\,\mathrm{d}\mu'\,\mathrm{d}\mu \\ &\quad - \frac{F_0}{4}\omega_0\,\mathrm{e}^{-\tau/\mu_0}\int_0^1 p(\mu;\mu_0)\,\mathrm{d}\mu \\ \frac{\mathrm{d}F^-}{\mathrm{d}\tau} &= \int_{-1}^0 \sum_{m=0}^{\infty} i_m P_m(\mu)\,\mathrm{d}\mu - \frac{\omega_0}{2}\int_{-1}^0\int_{-1}^1 p(\mu;\mu')\sum_{m=0}^{\infty} i_m P_m(\mu)\,\mathrm{d}\mu'\,\mathrm{d}\mu \\ &\quad + \frac{F_0}{4}\omega_0\gamma_4\,\mathrm{e}^{-\tau/\mu_0}\int_{-1}^0 p(\mu;\mu_0)\,\mathrm{d}\mu. \end{aligned} \right. \tag{A1.5}$$

Decomposing the zenith-to-nadir integrals into integrals over the up and down hemispheres leads to

$$\begin{cases} \dfrac{\mathrm{d}F^+}{\mathrm{d}\tau} = \displaystyle\int_0^1 \sum_{m=0}^{\infty} i_m P_m(\mu)\,\mathrm{d}\mu + \underbrace{\frac{\omega_0}{2}\int_0^1\int_0^1 p(\mu;\mu') \sum_{m=0}^{\infty} i_m P_m(\mu)\,\mathrm{d}\mu'\,\mathrm{d}\mu}_{\text{diffuse-beam forescatter}} \\ \qquad \underbrace{-\frac{\omega_0}{2}\int_0^1\int_{-1}^0 p(\mu;\mu') \sum_{m=0}^{\infty} i_m P_m(\mu)\,\mathrm{d}\mu'\,\mathrm{d}\mu}_{\text{diffuse-beam backscatter}} \underbrace{-\frac{F_0}{4}\omega_0\,\mathrm{e}^{-\tau/\mu_0}\int_0^1 p(\mu;\mu_0)\,\mathrm{d}\mu}_{\text{direct-beam backscatter}} . \\ \dfrac{\mathrm{d}F^-}{\mathrm{d}\tau} = \displaystyle\int_{-1}^0 \sum_{m=0}^{\infty} i_m P_m(\mu)\,\mathrm{d}\mu + \underbrace{\frac{\omega_0}{2}\int_{-1}^0\int_0^1 p(\mu;\mu') \sum_{m=0}^{\infty} i_m P_m(\mu)\,\mathrm{d}\mu'\,\mathrm{d}\mu}_{\text{diffuse-beam backscatter}} \\ \qquad \underbrace{+\frac{\omega_0}{2}\int_{-1}^0\int_{-1}^0 p(\mu;\mu') \sum_{m=0}^{\infty} i_m P_m(\mu)\,\mathrm{d}\mu'\,\mathrm{d}\mu}_{\text{diffuse-beam forescatter}} \underbrace{+\frac{F_0}{4}\omega_0\,\mathrm{e}^{-\tau/\mu_0}\int_{-1}^0 p(\mu;\mu_0)\,\mathrm{d}\mu}_{\text{direct-beam forescatter}} . \end{cases} \tag{A1.6}$$

Equation (A1.6) can be simplified to

$$\begin{cases} \dfrac{\mathrm{d}F^+(\tau)}{\mathrm{d}\tau} = \gamma_1 F^+(\tau) - \gamma_2 F^-(\tau) - \dfrac{F_0}{4}\omega_0\gamma_3\,\mathrm{e}^{-\tau/\mu_0} \\ \dfrac{\mathrm{d}F^-(\tau)}{\mathrm{d}\tau} = \gamma_2 F^+(\tau) - \gamma_1 F^-(\tau) + \dfrac{F_0}{4}\omega_0\gamma_4\,\mathrm{e}^{-\tau/\mu_0} \end{cases} \tag{A1.7}$$

by approximating the integrals. As such, (A1.7) is in essence the general two-stream approximation where $\gamma_1, \ldots, \gamma_4$ depend on assumptions made about I and p, as well as on μ_0 and optical properties. General solutions to (A1.7) are given by (1.23) through (1.28) in the mainbody of this chapter.

Some two-stream approximations (e.g., Coakley and Chýlek 1975) work directly with the backscattered fractions in (A1.6). For diffuse-beam, the backscattered fraction is

$$\overline{\beta} = \frac{1}{2}\int_0^1\int_0^1 p(\mu;\mu') \sum_{m=0}^{\infty} i_m P_m(\mu)\,\mathrm{d}\mu'\,\mathrm{d}\mu . \tag{A1.8}$$

Expanding $p(\mu;\mu')$ using the addition theorem for spherical harmonics and

$$P_n(-\mu) = (-1)^n P_n(\mu) , \tag{A1.9}$$

(A1.8) becomes

$$\overline{\beta} = \frac{1}{2}\sum_{n=0}^{\infty}(-1)^n\omega_n \int_0^1 P_n(\mu)\,\mathrm{d}\mu \left\{ \sum_{m=0}^{\infty} i_m \int_0^1 P_n(\mu')P_m(\mu')\,\mathrm{d}\mu' \right\} , \tag{A1.10}$$

where ω_n are phase function expansion coefficients [note that $\omega_0 = 1$ as single scattering albedo appears explicitly in (A1.1)]. For isotropic irradiance, (A1.10) reduces to

$$\overline{\beta} = \frac{1}{2}\sum_{n=0}^{\infty}(-1)^n\omega_n \int_0^1 \int_0^1 P_n(\mu)P_n(\mu')\,\mathrm{d}\mu\,\mathrm{d}\mu' \tag{A1.11}$$

which can be shown to equal (Wiscombe and Grams 1976)

$$\overline{\beta}_{\mathrm{iso}} = \frac{1}{2} - \frac{1}{8\pi}\sum_{n=0}^{\infty}\left[\frac{\Gamma\left(n+\frac{1}{2}\right)}{\Gamma\left(n+2\right)}\right]^2 \omega_{2n+1}\,. \tag{A1.12}$$

For non-isotropic irradiance it can be shown (Barker 1994) that

$$\overline{\beta} = i_0\overline{\beta}_{\mathrm{iso}} + \frac{1}{4\sqrt{\pi}}\sum_{m=0}^{\infty}(-1)^m\left[\frac{\Gamma\left(m+\frac{1}{2}\right)}{\Gamma\left(m+2\right)}\right]\left(1-\frac{\omega_{2m+1}}{4m+3}\right)i_{2m+1}. \tag{A1.13}$$

Correspondingly, via a similar development (Wiscombe and Grams 1976), the backscatter function for direct-beam irradiance can be expressed as

$$\beta\left(\mu_0\right) = \frac{1}{2} - \frac{1}{4\sqrt{\pi}}\sum_{n=0}^{\infty}(-1)^n\left[\frac{\Gamma\left(n+\frac{1}{2}\right)}{\Gamma\left(n+2\right)}\right]\omega_{2n+1}P_{2n+1}(\mu_0). \tag{A1.14}$$

As another example, the Eddington approximation (Shettle and Weinman 1970) uses the first two Legendre terms and approximates I and p as

$$I(\mu) = i_0 + i_1\mu \tag{A1.15}$$

and

$$p\left(\mu_0,\mu'\right) = 1 + 3g\mu_0\mu'\,, \tag{A1.16}$$

where g is the asymmetry parameter. This is often paired with the delta approximation (see Joseph et al. 1976) where the phase function is assumed to be

$$p\left(\mu_0,\mu'\right) = 2f\delta\left(\mu_0-\mu'\right) + \left(1-f\right)\left(1+3g\mu_0\mu'\right)\,, \tag{A1.17}$$

where δ is Dirac's distribution, and it is often adequate to set $f = g^2$. With these approximations, standard solutions to the two-stream [(1.23) through (1.28)] can be used with the basic input transformed as

$$\begin{aligned} \tau' &= \left(1-\omega_0 g^2\right)\tau\,, \\ \omega_0' &= \frac{1-g^2}{1-\omega_0 g^2}\omega_0\,, \\ g' &= \frac{g}{1+g}\,. \end{aligned} \tag{A1.18}$$

Table 1.1 gives parameter expressions for various common two-streams.

Table 1.1. References and parameter values for four common two-stream approximations. Note that by conservation of energy, $\gamma_3 = 1 - \gamma_4$

Method	Reference	γ_1	γ_2	γ_3
Eddington	Shettle + Weinman (1970)	$\frac{7-\omega_0(4+3g)}{4}$	$-\frac{1-\omega_0(4-3g)}{4}$	$\frac{2-3g\mu_0}{4}$
delta-Eddington	Joseph et al. (1976)	$\frac{7-\omega_0'(4+3g')}{4}$	$-\frac{1-\omega_0'(4-3g')}{4}$	$\frac{2-3g'\mu_0}{4}$
Coakley + Chýlek	Coakley + Chýlek (1975)	$2\left[1-\omega_0(1-\overline{\beta})\right]$	$2\omega_0\overline{\beta}$	$\beta\,(\mu_0)$
PIFM	Zdunkowski et al. (1980)	$\frac{8-\omega_0(5+3g)}{4}$	$\frac{3}{4}\omega_0'(1-g')$	$\frac{2-3g'\mu_0}{4}$

References

Aires, F. and W. B. Rossow, 2003: Inferring instantaneous, multivariate and nonlinear sensitivities for the analysis of feedback processes in a dynamical system: The Lorenz model case study. *Quart. J. Roy. Meteor. Soc.*, **129**, 239–275.

Astin, I., L. Di Girolamo, and H. M. van de Poll, 2001: Bayesian confidence intervals for true fractional coverage from finite transect measurements: Implications for cloud studies from space. *J. Geophys. Res.,* **106**, 17,303–17,310.

Barker, H. W. and J. A. Davies, 1992: Solar radiative fluxes for broken cloud fields above reflecting surfaces. *J. Atmos. Sci.*, **49**, 749–761.

Barker, H. W., 1994: A paremeterization and generalization of backscatter functions for two-stream approximations. *Beitr. Phys. Atmosph.*, **67**, 195–199.

Barker, H. W., 1996: A parameterization for computing grid-averaged solar fluxes for inhomogeneous marine boundary layer clouds. Part I: Methodology and homogeneous biases. *J. Atmos. Sci.*, **53**, 2289–2303.

Barker, H. W., B. A. Wielicki, and L. Parker, 1996: A parameterization for computing grid-averaged solar fluxes for inhomogeneous marine boundary layer clouds. Part II: Validation using satellite data. *J. Atmos. Sci.*, **53**, 2304–2316.

Barker, H. W., J.-J Morcrette, and G.D. Alexander, 1998: Broadband solar fluxes and heating rates for atmospheres with 3D broken clouds. *Q. J. R. Meteorol. Soc.*, **124**, 1245–1271.

Barker, H. W., G. L. Stephens, and Q. Fu, 1999: The sensitivity of domain-averaged solar fluxes to assumptions about cloud geometry. *Q. J. R. Meteorol. Soc.*, **125**, 2127–2152.

Barker, H. W., R. Pincus, and J.-J. Morcrette, 2002: The Monte Carlo Independent Column Approximation: Application within large-scale models. Proceedings from the GCSS workshop, Kananaskis, Alberta, Canada, May 2002. Available at: http://www.met.utah.edu/skrueger/gcss-2002/Extended-Abstracts.pdf.

Barker, H. W., and co-authors, 2003: Assessing 1D atmospheric solar radiative transfer models: Interpretation and handling of unresolved clouds. *J. Climate*, **16**, 2676–2699.

Barker, H. W. and P. Räisänen, 2005: Radiative sensitivities for cloud structural properties that are unresolved by conventional GCMs. *Q. J. R. Meteorol. Soc.*, **131**, 3103–3122.

Barker, H. W. and A. B. Davis, 2005: Approximation methods in atmospheric 3D radiative transfer, Part 2: Unresolved variability and climate applications. In *3D Radiative Transfer in Cloudy Atmospheres*, A. Marshak and A. B. Davis, Eds., Springer, Heidelberg, 686 pp.

Barker, H. W., 2005: Broadband irradiances and heating rates for cloudy atmospheres. In *3D Radiative Transfer in Cloudy Atmospheres*, A. Marshak and A. B. Davis, Eds., Springer, Heidelberg, 686 pp.

Benner, T. C. and K. F. Evans, 2001: Three-dimensional solar radiative transfer in small tropical cumulus fields derived from high-resolution imagery. *J. Geophys. Res.*, **106**, 14975–14984.

Bergman, J. W. and P. J. Rasch, 2002: Parameterizing vertically coherent cloud distributions. *J. Atmos. Sci.*, **59**, 2165–2182.

Bitz, C. M., J. C. Fyfe, and G. M. Flato, 2002: Sea ice response to wind forcing from AMIP models. *J. Climate*, **15**, 522–536.

Bony, S., J.-L. Dufresne, H. Le Treut, J.-J. Morcrette, and C. Senior, 2004: On dynamic and thermodynamic components of cloud changes. *Clim. Dyn.*, **22**, 71–86.

Briegleb, B. P., P. Minnis, V. Ramanathan, and E. Harrison, 1986: Comparison of regional clear-sky albedos inferred from satellite observations and model computations. *J. Clim. and Appl. Meteor.*, **25**, 214–226.

Cahalan, R. F., 1989: Overview of fractal clouds. In *Advances in Remote Sensing.* Deepak Publ., p. 371–389, 515 pp.

Cahalan, R. F., W. Ridgway, W. J. Wiscombe, T. L. Bell, and J. B. Snider, 1994: The albedo of fractal stratocumulus clouds. *J. Atmos. Sci.*, **51**, 2434–2455.

Cahalan, R. F., D. Silberstein, and J. Snider, 1995: Liquid water path and plane-parallel albedo bias during ASTEX. *J. Atmos. Sci.*, **52**, 3002–3012.

Cairns, B, A. A. Lacis, and B. E. Carlson, 2000: Absorption within inhomogeneous clouds and its parameterization in general circulation models. *J. Atmos. Sci.*, **57**, 700–714.

Cess, R. D., and others, 1993: Intercomparison of CO2 radiative forcing in atmospheric general circulation models. *Science*, **262**, 1252–1255.

Chambers, L. H., B. A. Wielicki, and K. F. Evans, 1997: Accuracy of the independent pixel approximation for satellite estimates of oceanic boundary layer cloud optical depth. *J. Geophys. Res.*, **102,** 1779–1794.

Charney, J., W. J. Quirk, S.-H. Chow, and J. Kornfield, 1977: A comparative study of the effects of albedo change on drought in semi-arid regions. *J. Atmos. Sci.*, **34**, 1366–1385.

Clothiaux, E. E., and co-authors, 1999: The atmospheric radiation measurement program cloud radars: Operational modes. *J. Atmos. and Ocean. Tech.*, **16**, 819–827.

Clothiaux, E. E., H. W. Barker, and A. V. Korolev, 2005: Observing clouds and their optical properties. In *3D Radiative Transfer in Cloudy Atmospheres*, A. Marshak and A. B. Davis, Eds., Springer, Heidelberg, 686 pp.

Coakley, J. A., Jr., and P. Chýlek, 1975: The two-stream approximation in radiative transfer: Including the angle of the incident radiation. *J. Atmos. Sci.*, **32**, 409–418.

Cole, J. N. S., H. W. Barker, W. O'Hirok, E. E. Clothiaux, M. F. Khairoutdinov, and D. A. Randall, 2005a: Atmospheric radiative transfer through global arrays of 2D clouds. *Geophys. Res. Lett.,* **32**, L19817, doi: 10.1029/2005GL023329.

Cole, J. N. S., H. W. Barker, D. A. Randall, M. F. Khairoutdinov, and E. E. Clothiaux, 2005b: Global consequences of interactions between clouds and radiation at scales unresolved by global climate models. *Geophys. Res. Lett.*, **32**, L06703, doi:10.1029/2004GL020945.

Cox, C. and W. Munk, 1956: Slopes of the sea surface deduced from photographs of the sun glitter. *Bull. Scripps Inst. Oceanog.*, **6**, 401–488.

Davis, A., P. Gabriel, S. Lovejoy, D. Schertzer, and G. Austin, 1990: Discrete angle radiative transfer – Part III: Numerical results and applications. *J. Geophys. Res.*, **95,** 11,729–11,742.

Evans, K. F. and A. Marshak, 2005: Numerical methods. In *3D Radiative Transfer in Cloudy Atmospheres*, A. Marshak and A. B. Davis, Eds., Springer, Heidelberg, 686 pp.

Fouquart, Y., B. Bonnel, and V. Ramaswamy, 1991: Intercomparing shortwave radiation codes for climate studies. *J. Geophys. Res.*, **96**, 8955–8968.

Fu, Q. and K.-N. Liou, 1992: On the correlated k-distribution method for radiative transfer in inhomogeneous atmospheres. *J. Atmos. Sci.*, **49**, 2139–2156.

Fu, Q., S. K. Krueger, and K.-N. Liou, 1995: Interactions of radiation and convection in simulated tropical cloud clusters. *J. Atmos. Sci.*, **52**, 1310–1328.

Geleyn, J. -F. and A. Hollingsworth, 1979: An economical analytical method for the computation of the interaction between scattering and line absorption of radiation. *Cont. Atmos. Phys.*, **52**, 1–16.

Grabowski, W. W., 2001: Coupling cloud processes with the large-scale dynamics using the cloud-resolving convection parameterization (CRCP), *J. Atmos. Sci.*, **58**, 978–997.

Gradshteyn, I. S. and Ryzhik, I. M. 1980: *Table of Integrals, Series, and Products: Corrected and enlarged edition*. Academic Press, London, 1160 pp.

Gregory, J. M. and co-authors, 2004: A new method for diagnosing radiative forcing and climate sensitivity. *Geophys. Res. Lett.*, **31**, L03205, doi:10.1029/2003GL018747.

Gu, Y. and K.-N. Liou, 2001: Radiation parameterization for three-dimensional inhomogeneous cirrus clouds: Application to climate models. *J. Climate*, **14**, 2443–2457.

Hansen, J. E., D. Russell, D. Rind, P. Stone, A. Lacis, L. Travis, S. Lebedeff, and R. Ruedy, 1983: Efficient three-dimensional global models for climate studies: Models I and II. *Mon. Wea. Rev.*, **111**, 609–662.

Hapke, B. W., 1981: Bidirectional reflectance spectroscopy I. Theory. *J. Geophys. Res.*, **86**, 3039–3054.

Hogan, R. J. and A. J. Illingworth, 2000: Derived cloud overlap statistics from radar. *Q. J. R. Meteorol. Soc.*, **126**, 2903–2909.

Houghton, J. T., and co-editors, 2001: *Climate Change 2001: The Scientific Basis*. Cambridge University Press, 881 pp.

Joseph, J. H., W. J. Wiscombe, and J. A. Weinman, 1976: The delta-Eddington approximation for radiative transfer. *J. Atmos. Sci.*, **33**, 2452–2459.

Khairoutdinov, M. F. and D. A. Randall, 2001: A cloud-resolving model as a cloud parameterization in the NCAR Community Climate System Model: Preliminary results. *Geophys. Res. Lett.,* **28,** 3617–3620.

Khairoutdinov, M. F. and D. A. Randall, 2003: Cloud resolving modeling of the ARM summer 1997 IOP: Model formulation, results, uncertainties, and sensitivities, *J. Atmos. Sci.*, **60**, 607–625.

King, M. D. and Harshvardhan, 1986: Comparative accuracy of selected multiple scattering approximations, *J. Atmos. Sci.*, **43**, 784–801.

Kreyscher, M., M. Harder, P. Lemke, and G. M. Flato, 2000: Results of the Sea Ice Model Intercomparison Project: Evaluation of sea-ice rheology schemes for use in climate simulations. *J. Geophys. Res.*, **105**, 11299–11320.

Li, J. and V. Ramaswamy, 1996: Four-stream spherical harmonic expansion approximation for solar radiative transfer. *J. Atmos. Sci.*, **53**, 1174–1186.

Li, J. and H. W. Barker, 2002: Accounting for unresolved clouds in a 1D infrared radiative transfer model. Part II: Horizontal variability of cloud water path. *J. Atmos. Sci.*, **59**, 3321–3339.

Li. J., J. S. Dobbie, P. Räisänen, and Q. Min, 2005: Accounting for unresolved cloud in solar radiation. *Q. J. Royal Meteorol. Soc.*, **131**, 1607–1629.

Liou, K. -N., 1992: *Radiation and Cloud Processes in the Atmosphere*. Oxford University Press, New York, 487 pp.

Loeb, N. G., K. Loukachine, B. A. Wielicki, and D. F. Young, 2003: Angular distribution models for top-of-atmosphere flux estimation from the Clouds and the Earth's Radiant Energy System instrument on the Tropical Rainfall Mission Satellite. Part II: Validation. *J. Appl. Meteorol.*, **42**, 1748–1769.

Lovelock, J., 1988: *The Ages of Gaia*. W. W. Norton and Co., New York, USA, ISBN 0-393-02583-7, 252 pp.

Mace, G. G. and S. Benson-Troth, 2002: Cloud-layer overlap characteristics derived from long-term cloud radar data. *J. Climate*, **15**, 2505–2515.

McFarlane, N. A., G. J. Boer, J.-P. Blanchet, M. Lazare, 1992: The Canadian Climate Centre second-generation general circulation model and its equilibrium climate. *J. Climate*, **5**, 1013–1044.

McKee, T. B. and S. K. Cox, 1974: Scattering of visible radiation by finite clouds. *J. Atmos. Sci.*, **31**, 1885–1892.

Meador, W. E. and W. R. Weaver, 1980: Two-stream approximations to radiative transfer in planetary atmospheres: A unified description of existing methods and a new improvement. *J. Atmos. Sci.*, **37**, 630–643.

Monahan, E. C. and I. G. O'Muircheartaigh, 1987: Comments on 'Albedos and glitter patterns of a wind-roughened sea surface'. *J. Phys. Oceanogr.*, **17**, 549–550.

O'Hirok, W. and C. Gautier, 1998: A three-dimensional radiative transfer model to investigate the solar radiation within a cloudy atmosphere. Part I: Spatial effects. *J. Atmos. Sci.*, **55**, 2162–2179.

O'Hirok, W. and C. Gautier, 2005: The impact of model resolution on differences between independent column approximation and Monte Carlo estimates of shortwave surface irradiance and atmospheric heating rate, *J. Atmos. Sci.*, **62**, 2939–2951.

Oreopoulos, L. and R. Davies, 1998: Plane parallel albedo biases from satellite observations. Part I: Dependence on resolution and other factors. *J. Climate*, **11**, 919–932.

Oreopoulos, L. and H. W. Barker, 1999: Accounting for subgrid-scale cloud variability in a multi-layer, 1D solar radiative transfer algorithm. *Q. J. R. Meteorol. Soc.,* **125**, 301–330.

Otterman, J., 1984: Albedo of a forest modeled as a plane of dense protrusions. *J. Atmos. Sci.*, **23**, 297–307.

Payne, R. E., 1972: Albedo of the sea surface. *J. Atmos. Sci.*, **29**, 959–970.

Pincus, R., S. A. MacFarlane, and S. A. Klein, 1999: Albedo bias and the horizontal variability of clouds in subtropical marine boundary layers: Observations from ships and satellites. *J. Geophys. Res.*, **104**, 6183–6191.

Pincus, R., H. W. Barker, and J.-J. Morcrette, 2003: A new radiative transfer model for use in GCMs. *J. Geophys. Res.*, **108**(D13), 4376, doi:10.1029/2002JD003322.

Pinty, B., T. Lavergne, R. E. Dickenson, J.-L. Widlowski, N. Gobron, and M. M. Verstrate, 2006: Simplifying the interaction of land surfaces with radiation for related remote sensing products to climate models. *J. Geophys. Res.*, **111**, D02116, doi:10.1029/2005JD005952.

Preisendorfer, R. W. and C. D. Mobley, 1986: Albedos and glitter patterns of a wind-roughened sea surface. *J. Phy. Oceanogr.*, **16**, 1293–1316.

Räisänen, P., H. W. Barker, M. Khairoutdinov, J. Li, and D. A. Randall, 2004: Stochastic generation of subgrid-scale cloudy columns for large-scale models. *Quart. J. Roy. Meteor. Soc.*, **130**, 2047–2067.

Räisänen, P. and H. W. Barker, 2004: Evaluation and optimization of sampling errors for the Monte Carlo independent column approximation. *Quart. J. Roy. Meteorol. Soc.*, **130**, 2069–2086.

Räisänen, P., H. W. Barker and J. Cole, 2005: The Monte Carlo Independent Column Approximation's conditional random noise: Impact on simulated climate. *J. Climate*, **17**, 4715–4730.

Randall, D., M. Khairoutdinov, A. Arakawa and W. Grabowski, 2003: Breaking the cloud parameterization deadlock. *Bull. Am. Met. Soc.*, **84**, 1547–1564.

Ronnholm, K., M. B. Baker, and H. Harrison, 1980: Radiative transfer through media with uncertain or variable parameters. *J. Atmos. Sci.*, **37**, 1279–1290.

Ross, J., 1981: *The Radiation Regime and Architecture of Plant Stands*. Dr. W. Junk, Norwell, MA, 391 pp.

Rossow, W. B., C. Delo, and B. Cairns, 2002: Implications of the observed mesoscale variations of clouds for the Earth's radiation budget. *J. Climate*, **15**, 557–585.

Schlesinger, M. E. and J. F. B. Mitchell, 1987: Climate model simulations of the equilibrium climatic response to increased carbon dioxide. *Review of Geophys.*, **4**, 760–798.

Schneider, W. H., 1972: Cloudiness as a global climatic feedback mechanism: The effects on the radiation balance and surface temperature of variations in cloudiness. *J. Atmos. Sci.*, **29**, 1413–1422.

Shettle, E. P. and J. A. Weinman, 1970: The transfer of solar irradiance through inhomogeneous turbid atmospheres evaluated by Eddington's approximation. *J. Atmos. Sci.*, **27**, 1048–1055.

Snyder, P. K., J. A. Foley, M. H. Hitchman, and C. Delire, 2004: Analyzing the effects of complete tropical foret removal on the regional climate using a detailed three-dimensional energy budget: An application to Africa. *J. Geophys. Res.*, **109**, D211102, doi: 10.1029/2003JD004462.

Stamnes, K., S.-C. Tsay, W. J. Wiscombe, and K. Jayaweera, 1988: A numerically stable algorithm for discrete-ordinate-method radiative transfer in multiple scattering and emitting layered media. *Appl. Opt.*, **27**, 2502–2509.

Stephens, G. L., 1988: Radiative transfer through arbitrary shaped optical media: Part II: Group theory and simple closures. *J. Atmos. Sci.*, **45**, 1837–1848.

Stephens, G. L., P. M. Gabriel, and S.-C. Tsay, 1991: Statistical radiative transfer in one-dimensional media and its application to the terrestrial atmosphere. *Trans. Theory Stat. Phys.*, **20**, 139–175.

Stephens, G. L., and co-authors, 2002: The CloudSat mission and the A-train: A new dimension of space-based observations of clouds and precipitation. *Bull. Amer. Meteorol. Soc.*, **83**, 1771–1790.

Stephens, G. L., N. B. Wood, and P. M. Gabriel, 2004: An assessment of the parameterization of subgrid-scale cloud effects on radiative transfer. Part I: Vertical overlap. *J. Atmos. Sci.*, **61**, 715–732.

Stokes, G. M. and S. E. Schwartz, 1994: The atmospheric radiation measurement (ARM) program: Programmatic background and design of the cloud and radiation test bed. *Bull. Amer. Meteor. Soc.*, **75**, 1201–1221.

Stowasser, M., K. Hamilton, and G. J. Boer, 2006: Local and global climate feedbacks in models with differing climate sensitivities. *J. Climate*, **19**, 193–209.

Tiedtke, M., 1996: An extension of cloud-radiation parameterization in the ECMWF model: The representation of subgrid-scale variations of optical depth. *Mon. Wea. Rev.*, **124**, 745–750.

Verstraete, M. M., 1987: Radiation transfer in plant canopies: Transmission of direct solar radiation and the role of leaf orientation. *J. Geophys. Res.*, **92**, 10,985–10,995.

Warren, S. G., 1982: Optical properties of snow. *Rev. Geophys. Space Phys.*, **20**, 67–89.

Warren, S. G., R. E. Brandt, and P. O'Rawe-Hinton, 1998: Effect of surface roughness on bidirectional reflectance of Antarctic snow. *J. Geophys. Res.*, **103**, 25,789–25,807.

Webb, M., C. Senior, S. Bony, and J.-J. Morcrette, 2001: Combining ERBE and ISCCP data to assess clouds in the Hadley Centre, ECMWF, and LMD atmospheric climate models. *Clim. Dyn.*, **17**, 905–922.

Welch, R. M and B. A. Wielicki, 1985: A radiative parameterization of stratocumulus cloud fields. *J. Atmos. Sci.*, **42**, 2888–2897.

Wiscombe, W .J. and G. W. Grams, 1976: The backscattered fraction in two-stream approximations. *J. Atmos. Sci.,* **33**, 2440–2451.

Wiscombe, W. J., 1977: The delta-Eddington approximation for a vertically inhomogeneous atmosphere. NCAR Tech. Note, TN-121+STR, 66 pp.

Zdunkowski, G. W., R. M. Welch, and G. Korb, 1980: An investigation of the structure of typical two-stream methods for the calculation of solar fluxes and heating rates. *Contr. Atmos. Phys.*, **53**, 147–166.